*American Mineralogist, Volume 105, pages 1472–1489, 2020*

# Structural and spectroscopic study of the kieserite-dwornikite solid-solution series, $(Mg,Ni)SO_4 \cdot H_2O$, at ambient and low temperatures, with cosmochemical implications for icy moons and Mars

**Dominik Talla[1,*,†], Madeleine Balla[1], Claudia Aicher[1], Christian L. Lengauer[1], and Manfred Wildner[1]**

[1]Institut für Mineralogie und Kristallographie, Althanstrasse 14, 1090 Wien, Austria

## Abstract

The investigation of the presence and role of sulfates in our solar system receives growing attention because these compounds play a crucial role in the water budget of planets such as Mars and significantly influence melting equilibria on the icy moons of Saturn and Jupiter, leading to the formation of subsurface oceans and even cryovolcanism. Despite the dominant presence of higher sulfate hydrates such as epsomite, $MgSO_4 \cdot 7H_2O$, and mirabilite, $Na_2SO_4 \cdot 10H_2O$, on these moons' surfaces, it is not excluded that lower-hydrated sulfates, such as kieserite, $MgSO_4 \cdot H_2O$, are also present, forming from higher hydrates under pressures relevant to the mantle of the icy moons. Given the composition of the soluble fraction in C1 and C2 chondritic meteorites, which are high in Ni content and also considered to represent the composition of the rocky cores of the Jovian icy moons, the actual compositions of potentially present monohydrate sulfates likely lie at intermediate values along the solid-solution series between kieserite and transition-metal kieserite-group end-members, incorporating Ni in particular. Moderate Ni contents are also probable in kieserite on Mars due to the planet's long-term accumulation of meteoritic nickel, although likely to a much lesser extent than Fe.

Structural and spectroscopic differences between the pure Mg- and Ni-end-members have been previously documented in the literature, but no detailed crystal chemical and spectroscopic investigation along the Mg-Ni solid solution has been done yet. The present work proves the existence of a continuous $(Mg,Ni)SO_4 \cdot H_2O$ solid-solution series for the first time. It provides a detailed insight into the changes in lattice parameters, structural details, and positions of prominent bands in infrared (transmission, attenuated total reflectance, diffuse reflectance) and Raman spectra in synthetic samples as the Ni/Mg ratio progresses, at both ambient as well as low temperatures relevant for the icy moons and Mars. UV-Vis-NIR crystal field spectra of the Ni end-member also help to elucidate the influence of $Ni^{2+}$-related bands on the overtone- and combination modes.

The $(Mg,Ni)SO_4 \cdot H_2O$ solid-solution series shows Vegard-type behavior, i.e., lattice parameters as well as spectral band positions, change along linear trends with increasing Ni content. Infrared spectra reveal significant changes in the wavenumber positions of prominent bands, depending on the Ni/Mg ratio. We show that the temperature during measurement also has an influence on band position, mainly in the case of $H_2O$-related bands. The changes observed for several absorption features in the IR spectra enable rough estimation of the Ni/Mg ratio in the monohydrate sulfate, which is applicable to present and future remote sensing data, as well as in situ measurements on Mars or the icy moons. The spectral features most diagnostic of composition are the vibrational stretching modes of the $H_2O$ molecule and a band unique to kieserite-group compounds at around 900 $cm^{-1}$ in the IR spectra, as well as the pronounced $\nu_3$ and $\nu_1$ sulfate stretching modes visible in Raman spectra.

**Keywords:** Kieserite-dwornikite solid solution, icy satellites, Mars, crystal chemistry, FTIR spectroscopy, Raman spectroscopy, UV-Vis-NIR spectroscopy; Volatile Elements in Differentiated Planetary Interiors

## Introduction

The past few decades of planetary exploration uncovered the presence of considerable amounts of sulfates in our solar system. From the surface (and subsurface) of Mars to the icy moons of Jupiter and Saturn and even veinlets in chondritic meteorites, sulfates of Mg, Fe, Mn, and Ni represent an important constituent of planetary and meteoritic material (Frederiksson and Kerridge 1988; Burgess et al. 1991; Kargel 1991). The existence of sulfate deposits containing kieserite within layered terrains on Mars is now well established (e.g., Bishop et al. 2009; Noel et al. 2015; Mangold et al. 2008; Lichtenberg et al. 2010), most probably as a solid solution between kieserite ($MgSO_4 \cdot H_2O$) and szomolnokite ($FeSO_4 \cdot H_2O$). Minor Ni-contents are suggested by Papike et al. (2007), who note that Martian kieserite, via partial Fe-, Ni-, or Co-incorporation, could be an indicator for meteorite impacts as relevant processes in the formation and redistribution

* E-mail: dominik.talla@univie.ac.at

† Special collection papers can be found online at http://www.minsocam.org/MSA/AmMin/special-collections.html.

0003-004X/20/0010–1472$05.00/DOI: https://doi.org/10.2138/am-2020-7287

of sulfates on Mars. Moreover, Knauth et al. (2005) suggest that the observed sulfate-cemented sedimentary structures could be ascribed to impact surges from a large nickel-iron meteorite.

Hydrated Mg-sulfates as alteration products are known from C1 and C2 type carbonaceous chondrites, making up to 73% by mass of their soluble fraction (Frederiksson and Kerridge 1988; Burgess et al. 1991). The identification of higher-hydrated Na- and Mg-sulfates on the surface of Jupiter's moons Ganymede and Europa is another important discovery (McCord et al. 2001; Dalton et al. 2005, 2012). The formation of $MgSO_4$-$H_2O$-$Na_2SO_4$ low-temperature eutectic brines is believed to be essential for the existence of crustal rifting, cryovolcanism (both active and extinct), or the presence of subsurface oceans on Jupiter's and Saturn's icy satellites (Kargel 1991; McCord et al. 2001). Such oceans could theoretically sustain or have sustained extraterrestrial life in the past (Kargel et al. 2000; McKinnon and Zolensky 2003; Spencer et al. 2009 and citations therein; Solomonidou et al. 2011). Active cryovolcanism, owing its existence to tidal heating, is now well documented from the south-polar region of Saturn's moon Enceladus (Spencer et al. 2009). All of these sulfates could have Ni substitution in their structures, and if they are monohydrated, their composition could be identified with the research we present in this work.

The high sulfate hydration states interpreted to be present on the surface of icy moons could be modified by interaction with cosmic radiation. For example, epsomite decomposes to kieserite (Jamieson et al. 2014), the thermodynamic stability of which is strongly enhanced by the surrounding vacuum (Zolotov and Shock 2001). The models of fractional eutectic melting indicate the evolution of a Mg-sulfate precipitate ("salty ice") in the high-pressure ice mantle region of the large icy satellites, potentially consisting also of lower sulfate hydrates (Kargel 1991; Nakamura and Ohtani 2011). Due to its higher buoyancy, this salty ice mixture is believed to ascend upward, supplying soluble salts to the overlying ocean (Journaux et al. 2017), thus providing nutrients for the potential evolution of extraterrestrial life (Vance et al. 2014). The basic stability of kieserite and isostructural sulfate monohydrates of transition metals in such high-pressure environments, albeit modified by displacive second-order phase transitions, is supported by recent investigations (Meusburger et al. 2018, 2019; Ende et al. 2019a, 2019b).

The rocky cores of the icy moons of the gas giants, from which the salts now present in their oceans and upper ice layers originated, probably correspond in composition to C1 or C2 chondritic material and contain sulfates of Mg, Mn, and Ni in the soluble fraction (Burgess et al. 1991; Kargel 1991). As such, the actual composition of monohydrated sulfate, should it be present, will likely represent an intermediate value between kieserite ($MgSO_4 \cdot H_2O$) and its isostructural transition-metal-bearing compounds, in particular with Ni- and Mn-contents (Frederiksson and Kerridge 1988; Anders and Grevese 1989).

Despite the knowledge of significant changes in lattice parameters and IR spectra between kieserite and the Ni-end-member dwornikite (Wildner and Giester 1991; Stoilova and Lutz 2002; Stoilova 2003), no detailed investigation of the structural and spectroscopic behavior along the Mg-Ni solid-solution series has been conducted. A structural and crystal-chemical study was recently published by Bechtold and Wildner (2016) for the kieserite-cobaltkieserite series, followed by a thorough examination including spectroscopic results of the kieserite-szomolnokite solid solution, $Mg_{1-x}Fe_xSO_4 \cdot H_2O$, by Talla and Wildner (2019).

In this paper, we present the results of detailed structural, crystal chemical, Fourier transform infrared (FTIR), and Raman-spectroscopic investigations on synthetically prepared members along the binary kieserite-dwornikite solid solution, $Mg_{1-x}Ni_xSO_4 \cdot H_2O$, at ambient and lower temperatures, as relevant for surface conditions of Mars and icy satellites of Jupiter and Saturn, complemented by ultraviolet-visible-near infrared (UV-Vis-NIR) crystal field spectra of $Ni^{2+}$ in dwornikite. The presented data may prove valuable in further refining the chemical composition of kieserite present on extraterrestrial bodies in our solar system based on available remote sensing data in the mid-infrared range, as well as providing a fundamental data set for interpretation of future data of in situ measurements by landers and rovers.

Note that throughout the present paper we use the name "dwornikite," originally describing a mineral with approximate composition $(Ni_{0.9}Fe_{0.1})SO_4 \cdot H_2O$ (Milton et al. 1982), to refer to the pure $NiSO_4 \cdot H_2O$ end-member.

## Experimental methods

### Sample preparation

The evaporation technique was used to prepare powder sample material for the IR and Raman spectrocopic studies. Epsomite ($MgSO_4 \cdot 7H_2O$) was mixed with $NiSO_4 \cdot 6H_2O$ in the desired Mg/Ni molar ratio, amounting to 6 g in total (both chemicals were of analytical grade). The reagents were dissolved in a mixture of 80 mL of doubly distilled $H_2O$ and 10 mL 95% $H_2SO_4$ in a beaker. The solution was evaporated at 70 °C for 10 days, yielding a crust of pale green $(Mg,Ni)SO_4 \cdot H_2O$ at the bottom of the vessel, covered by the remaining concentrated acid. In addition, the following hydrothermal technique was used to synthesize coarse-grained samples, enabling selection of individual single crystals for X-ray diffraction and low-temperature Raman investigations. Teflon-lined (polytetrafluoroethylene) stainless steel autoclaves with an inner volume of ~2 $cm^3$ were filled with a mixture of epsomite ($MgSO_4 \cdot 7H_2O$) and $NiSO_4 \cdot 6H_2O$ amounting to 0.4 g in total with a pre-set Mg/Ni molar ratio. The solvent consisted of 0.7 mL distilled $H_2O$ and 2.2 mL concentrated $H_2SO_4$ (w = 0.95). All reagents were of analytical grade. An isothermal temperature run at 220 °C for a period of 14 days followed by cooling to room temperature within 4 days was used. Initial problems such as Ni preferably remaining in solution, synthesized crystals of inadequate size and polysynthetic twinning inherent to tightly sealed autoclaves (samples Ni5a to Ni40a), were largely resolved by applying the "leaking vessel approach." A small leak between the Teflon reaction vessel and its lid was allowed by only gently tightening the lid upon assembly. Through this leak, $H_2O$ slowly evaporated leading to slow precipitation of the monohydrate sulfates as an aggregate of single crystals, including individuals with sufficient quality and size.

Subsequent treatment of the product was the same for single crystals and powder material as follows. After decanting the fluid and mechanical removal of the solids from the reaction vessel, the product was rinsed twice with distilled $H_2O$, taking advantage of the sulfate's relatively slow dissolution rate. Thereafter, the crystals were washed using 98% ethanol to remove the $H_2O$ from the previous step, and the product was dried in an oven at 65 °C overnight, then stored in airtight vials.

### Chemical analyses and powder X-ray diffraction

Wet-chemical analyses were done on a part of each sample batch at the Masaryk University in Brno, Czech Republic. An amount of ~0.5 g of ground sample material was dissolved in boiling $HNO_3$ (w = 0.65). Contents of Mg and Ni were both determined spectrophotometrically (instrument Solaar M5—TJAsolutions, measurement time 4 s per element) with an analytical error of 0.005 wt% for Mg and 0.002 wt% for Ni.

A further part of each sample batch was examined using powder X-ray diffraction to confirm expected lattice parameter shifts along the solid solution and the mono-phase character of each batch. The material was pressed onto an Si-holder and measured on a Philips PW 3710 diffractometer, and data were collected from 5–120° 2θ in 0.2° increments with a collection time of 15 s per step. Following the phase identification with the program EVA2013, Rietveld refinements were performed with the Bruker program TOPAS3.

## Single-crystal X-ray diffraction

Single crystals suitable for X-ray diffraction measurements were selected by choosing individuals with homogeneous extinction under crossed polars. The crystal structures of 10 representatives along the $Mg_{1-x}Ni_xSO_4 \cdot H_2O$ solid-solution series, including the dwornikite end-member, were determined from diffraction data measured at 295 K with graphite-monochromatized Mo$K\alpha$ radiation on a Nonius Kappa CCD diffractometer equipped with a 0.3 mm monocapillary X-ray optics collimator. Complete Ewald spheres up to $2\theta = 80°$ were each collected in several sets of φ- and ω-scans with 2° rotation per CCD frame, at a crystal to detector distance of 30 mm. The integration and correction of the intensity data, including an absorption correction by multi-frame scaling and the refinement of lattice parameters, were done with the Nonius program DENZO-SMN.

Temperature-dependent X-ray data collections of the dwornikite end-member were performed between +40 and –160 °C in steps of 40 °C on a Bruker ApexII diffractometer equipped with a CCD area detector and an Incoatec Microfocus Source IμS (30 W, multilayer mirror, Mo$K\alpha$ radiation), in a dry stream of nitrogen (Cryostream 800, Oxford Cryosystems). Several sets of φ- and ω-scans with 2° scan width were measured at a crystal-detector distance of 40 mm up to 80° 2θ full sphere. Absorption was corrected by the evaluation of multi-scans. For the sake of data consistency, the lattice parameters extracted from the ApexII temperature-dependent measurements were corrected in such a way that the interpolated values at 20 °C match those obtained from the Nonius Kappa CCD room-temperature measurement of the very same dwornikite single crystal.

All structure refinements were performed on $F^2$ with SHELXL-97 (Sheldrick 2008) in the "traditional" non-reduced kieserite cell setting. Scattering curves for neutral atoms were used. The Mg/Ni ratios of the particular single crystals studied were extracted as a refined variable in the respective structure refinement runs.

CIF data[1] for room-temperature structures included in Tables 2 and 3 (plus CIF of end-member kieserite from Bechtold and Wildner 2016) and of temperature-dependent structure investigations included in Tables 4 and 5 have been deposited[1].

## IR spectroscopy

The general procedure followed that for the comparable investigations on the kieserite-szomolnokite solid solution by Talla and Wildner (2019). A part of each sample batch was ground by hand in an agate mortar. For our purposes, the obtained sample powder with the size of the largest crystallites not exceeding 100 μm did not have to be sieved or treated in any additional way since grain size influences only band amplitudes but not their wavenumber position (Jamieson et al. 2014). Fourier transform infrared (FTIR) measurements were conducted in transmission, attenuated total reflectance (ATR), and diffuse reflectance infrared Fourier transform (DRIFT) modes were done by means of the Bruker Tensor 27 FTIR spectrometer (Globar light source, KBr beam splitter, DTGS detector). For transmission measurements, the powdered sample material was diluted in KBr at a weight ratio of 1:300 and pressed into pellets with a vacuum press. ATR measurements were done using the mountable Bruker ATR unit by pressing the sample powder against the diamond surface. For DRIFT measurements, the powder was pressed into the appropriate sample holder of a Perkin–Elmer DRIFT unit. Finely ground MgO was used as the reflectivity standard for the background measurements. All reflectance data were converted via the Kubelka-Munk equation implemented in the Bruker OPUS software. The full wavenumber range (7000–400 $cm^{-1}$) was investigated in all analytical modes. The instrumental spectral resolution was 4 $cm^{-1}$. Each measurement was averaged from 50 individual scans to reduce noise. In the scope of the DRIFT analyses, each sample was measured in a pure state, as well as diluted with KBr in a ratio of 1:20, to enhance the absorption contribution to the resulting spectrum.

Low-temperature FTIR transmission measurements were done on KBr micropellets (2 mm aperture diameter in a steel gasket, sample dilution ratio 1:300) using a Linkam FTIR600 cooling stage equipped with KBr windows. Measurements were done in 40 K intervals ranging from 313 K (40 °C) down to 113 K (–160 °C). Some additional measurements at 93 K (–180 °C) were done occasionally.

Our usage of wavenumbers ν (in $cm^{-1}$) as the principal spectral unit in text and figures, as opposed to wavelengths λ (in μm), is justified by its direct proportionality to the energy of the incident photons. The corresponding wavelengths can be easily obtained via the formula $\lambda(\mu m) = 10000/\nu(cm^{-1})$.

## Raman spectroscopy

Raman spectra were measured on a Horiba Jobin Yvon LabRam–HR spectrometer, equipped with an Olympus BX41 optical microscope. The diffraction grating with 1800 grooves/mm and the 633 nm laser was chosen. The system is equipped with a Si-based, Peltier-cooled charge-coupled device (CCD) detector. A 100× objective (NA = 0.55) was used for all room-temperature measurements. The wavenumber accuracy was better than 0.5 $cm^{-1}$, and the spectral resolution was determined to be ~0.3 $cm^{-1}$. Room-temperature Raman spectra were acquired in tandem with DRIFT measurements (see above), taking advantage of the powdered material for IR spectroscopy already being contained within a convenient sample holder. All Raman spectra were acquired between 100–4000 $cm^{-1}$ shift, using multi-window scans with a counting time of 50 s per window and repeating every scan twice to eliminate spikes.

Low-temperature Raman measurements were conducted on single crystals using the Linkam FTIR 600 cooling stage. Despite varying and unknown crystal orientation, the use of single crystals with significantly better scattering, allowing shorter measuring times (5 s per window) was essential to mitigate ice buildup on the sample surface during cooling. The crystals were placed on the Ag-block of the cooling stage covered with a thermal conducting fluid. The bulky stage necessitated the use of a long-distance objective with a 50× magnification (focal distance 10.6 mm), with the same setup of the Raman instrument otherwise. The spectra were acquired in two separate spectral regions, from 100 to 1600 and from 2800 to 4000 $cm^{-1}$ shift. Most acquisition temperatures matched those used during FTIR temperature-dependent investigations to allow for direct comparison.

Band positions for both FTIR and Raman spectra were obtained by fitting the spectra with Voigt-shaped band profiles with the program Peakfit (Jandel Scientific, ver. 4.0). Initial estimates of the number of bands and their distribution in IR and Raman spectra were based on the investigations done on kieserite by previous authors (Stoilova and Lutz 1998; Lane 2007; Lane et al. 2015 for FTIR spectroscopy; and Chio et al. 2007 and citations therein, for Raman spectra). Linear regression analysis of FTIR and Raman data was accomplished using the inbuilt statistical module of the program SigmaPlot 13.

## UV-Vis-NIR spectroscopy and crystal field calculations

An unpolarized optical absorption spectrum of a single crystal of $NiSO_4 \cdot H_2O$ was measured at room temperature in the spectral range 32000–5000 $cm^{-1}$ on a mirror-optics microscope IRscope-II, attached to a Bruker IFS66v/S FT-spectrometer, using a measuring spot of 165 μm. A KBr beam splitter and appropriate combinations of light sources (Xe- or W-lamp) and detectors (GaP-, Si-, Ge-diodes) were used to cover the spectral range. The final spectrum is combined from three partial spectra (UV and Vis segments: 32000–10000 $cm^{-1}$, both at 40 $cm^{-1}$ spectral resolution and averaged from 512 scans; NIR: 10000–5000 $cm^{-1}$ at 20 $cm^{-1}$ spectral resolution, 256 scans). The UV and NIR spectral segments were each aligned in absorbance to match with the unadjusted Vis spectrum at 20000 and 10000 $cm^{-1}$, respectively, and then converted to the linear absorption coefficient α.

Crystal field (CF) calculations were performed with the HCFLDN2 module of the computer program package by Y.Y. Yeung (Chang et al. 1994), based both on classical CF parameters assuming a pseudotetragonal field (according to the octahedral [4+2] coordination) as well as in the framework of the semi-empirical Superposition Model (SM) of crystal fields. In the latter case, the reference metal–ligand distance $R_0$ was set to 2.06 Å, the mean <Ni–O> bond length in dwornikite, and some parameters were fixed to reduce the number of variables (namely $t_2 = 3$, i.e., the "electrostatic" value, and Racah $C/B = 4.2$, as obtained in the classical approach). For further details concerning the calculation procedures, the reader is referred to comparable approaches in Wildner et al. (2013) and respective references therein.

# Results

## Sample chemistry and powder X-ray diffraction

The wet chemical analyses yielded the actual Mg/Ni ratio in the synthesized bulk products in their respective final state, i.e., after the purification process by water and ethanol, described in the Experimental section. They revealed systematic differences between the pre-adjusted and the actual Mg/Ni ratio in the product. As is evident from Figure 1, the synthesis approach greatly influences the extent of discrepancy between pre-set and experimental $x_{Ni}$ values. Samples prepared by the evaporation technique show a convex trend with relative Ni depletion peaking in intermediate members of the solid solution. The few finely crystalline samples prepared in a fully sealed hydrothermal autoclave at 210 °C show pronounced Ni-deficiency with the major part of $Ni^{2+}$ remaining in solution. Details of the chemical

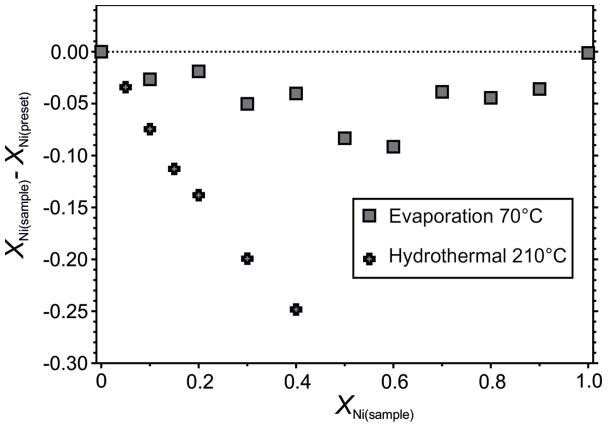


**Figure 1.** Deviations between actual Ni-content of the $Mg_{1-x}Ni_x(SO_4)\cdot H_2O$ solid solution samples used for spectroscopic investigations $x_{Ni(sample)}$ as determined by the wet chemical analyses and the preset Mg/Ni ratio in the batch $x_{Ni(preset)}$. Errors are equal or smaller than the symbol size. Note the strong Ni deficiency in the product with the hydrothermal technique in use (tightly sealed autoclave). This deviation led to the use the "leaking vessel approach" for synthesis of single crystals (not depicted), with the actual $x_{Ni}$ ratio refined from the single-crystal X-ray diffraction results.

composition of samples used for FTIR and Raman spectroscopy are presented in Table 1. The material obtained by the hydrothermal "leaking vessel approach" yielded larger crystals. Because this material was intended for single-crystal measurements, the Mg/Ni ratios of individual hand-picked crystals were extracted as a variable parameter in the respective structure refinements.

Powder X-ray diffraction measurements and Rietveld refinements confirmed that the batches consist nearly exclusively of kieserite-group $(Mg,Ni)SO_4\cdot H_2O$ phases; occasional traces of nickelhexahydrite were found. The diffraction patterns showed no signs of peak splitting or abnormal broadening, thus confirming compositional homogeneity and the mono-phase character of the obtained kieserite-group solid solutions.

**Table 1.** Composition of the studied samples as shown in Figure 1, determined by wet chemical analyses

| Sample ID | Mg (wt%) | Ni (wt%) | $x_{Ni(sample)}$ | $x_{Ni(preset)}$ | $x_{Ni(sample)}$-$x_{Ni(preset)}$ |
|---|---|---|---|---|---|
| Ni5a | 17.60 | 0.68 | 0.016 | 0.050 | –0.034 |
| Ni10a | 17.63 | 1.11 | 0.025 | 0.100 | –0.075 |
| Ni15a | 17.36 | 1.61 | 0.037 | 0.150 | –0.113 |
| Ni20a | 15.68 | 2.49 | 0.062 | 0.200 | –0.138 |
| Ni30a | 14.72 | 3.98 | 0.101 | 0.300 | –0.199 |
| Ni40a | 14.00 | 6.05 | 0.152 | 0.400 | –0.248 |
| Ni100a | 0.11 | 27.29 | 0.990 | 1.00 | 0.001 |
| Ni10aq | 16.74 | 3.20 | 0.073 | 0.100 | –0.027 |
| Ni20aq | 14.55 | 7.77 | 0.181 | 0.200 | –0.019 |
| Ni30aq | 12.32 | 9.90 | 0.250 | 0.300 | –0.050 |
| Ni40aq | 10.26 | 13.92 | 0.360 | 0.400 | –0.040 |
| Ni50aq | 8.40 | 14.48 | 0.417 | 0.500 | –0.083 |
| Ni60aq | 6.55 | 16.37 | 0.508 | 0.600 | –0.092 |
| Ni70aq | 4.66 | 21.96 | 0.661 | 0.700 | –0.039 |
| Ni80aq | 3.07 | 22.92 | 0.756 | 0.800 | –0.044 |
| Ni90aq | 1.47 | 22.60 | 0.864 | 0.900 | –0.036 |
| Ni100aq | 0.01 | 27.85 | 0.999 | 1.000 | –0.001 |

*Notes:* Deviations of the actual sample Ni content $x_{Ni(sample)}$ from the preset Mg/Ni ratio in the batch $x_{Ni(preset)}$ are also given. The analytical error amounts to 0.005 wt% for Mg and 0.002 wt% for Ni. Note that the Mg/Ni ratios of individual hand-picked crystals used for the single-crystal X-ray diffraction studies (from "leaking vessel" runs) were extracted as variable parameter in the respective structure refinement runs.

**Table 2.** Crystal data and details of X-ray data collections and structure refinements for selected representatives of the $Mg_{1-x}Ni_x(SO_4)\cdot H_2O$ solid-solution series

| $Mg_{1-x}Ni_x(SO_4)\cdot H_2O$ | $Mg_{1.00}Ni_{0.00}$ | $Mg_{0.76}Ni_{0.24}$ | $Mg_{0.48}Ni_{0.52}$ | $Mg_{0.24}Ni_{0.76}$ | $Mg_{0.00}Ni_{1.00}$ |
|---|---|---|---|---|---|
| $x_{Ni}$ | 0.0 | 0.236(2) | 0.525(2) | 0.759(2) | 1.0 |
| $a$ (Å) | 6.910(1) | 6.891(1) | 6.859(1) | 6.845(1) | 6.829(1) |
| $b$ (Å) | 7.634(2) | 7.622(1) | 7.620(1) | 7.614(1) | 7.605(1) |
| $c$ (Å) | 7.643(2) | 7.592(1) | 7.545(1) | 7.502(1) | 7.463(1) |
| β (°) | 118.00(1) | 117.98(1) | 117.84(1) | 117.80(1) | 117.75(1) |
| $V$ (Å$^3$) | 356.00(14) | 352.14(9) | 348.67(9) | 345.84(9) | 342.98(9) |
| μ (mm$^{-1}$) | 0.97 | 2.16 | 3.64 | 4.86 | 6.14 |
| $D_{calc}$ (g/cm$^3$) | 2.582 | 2.763 | 2.980 | 3.159 | 3.346 |
| Exposure time (s)/frame | 140 | 180 | 60 | 40 | 40 |
| CCD frames processed | 508 | 497 | 505 | 531 | 503 |
| Frame scale factors (max, min) | 1.11, 0.89 | 1.16, 0.77 | 1.21, 0.89 | 1.20, 0.72 | 1.18, 0.81 |
| Total number of intensity data | 12919 | 14225 | 16826 | 13763 | 11698 |
| Total number of reflections | 8865 | 8270 | 7928 | 8698 | 8191 |
| Intensity data for unit cell | 5101 | 7662 | 12062 | 6952 | 4887 |
| Number of *hkl* values | 3995 | 4052 | 4037 | 3995 | 3728 |
| Unique *hkl* values | 1089 | 1082 | 1071 | 1072 | 1056 |
| $R_i$ (%) | 3.20 | 3.66 | 2.94 | 3.53 | 2.60 |
| $F_o > 4\sigma(F_o)$ | 937 | 919 | 1005 | 1029 | 1019 |
| Variables | 39 | 42 | 42 | 42 | 40 |
| wR2 [for all $F_o^2$] (%) | 6.17 | 7.62 | 5.03 | 4.80 | 4.99 |
| Weighting parameters $a$, $b$[a] | 0.028, 0.20 | 0.021, 0.85 | 0.019, 0.30 | 0.024, 0.08 | 0.024, 0.52 |
| R1 [for $F_o > 4\sigma(F_o)$] (%) | 2.27 | 3.33 | 2.05 | 1.91 | 1.95 |
| R1 [for all $F_o$] (%) | 2.94 | 4.59 | 2.28 | 2.02 | 2.05 |
| Goodness of fit | 1.109 | 1.170 | 1.143 | 1.104 | 1.077 |
| Extinction coefficient | 0 | 0.002(2) | 0.010(2) | 0.016(2) | 0.023(2) |
| $\Delta\rho_{max, min}$ (e$^-$ Å$^{-3}$) | 0.47, –0.51 | 0.83, –0.44 | 1.02, –0.55 | 1.18, –0.77 | 0.78, –0.97 |

*Notes:* Common data: monoclinic, space group $C2/c$ (no. 15), $Z = 4$. Respective data for end-member kieserite are reproduced from Bechtold and Wildner (2016).
[a] $w = 1/[\sigma^2(F_o^2) + (a \times P)^2 + b \times P]$; $P = \{[\max \text{ of } (0 \text{ or } F_o^2)] + 2F_c^2\}/3$.

## Crystal structures

Crystal data and details of the data collections and structure refinements of four selected representatives of the $Mg_{1-x}Ni_xSO_4\cdot H_2O$ solid solution, including the dwornikite end-member, are summarized in Table 2, respective final atomic coordinates and displacement parameters are listed in Table 3. Corresponding temperature-dependent data of the dwornikite end-member are compiled for three selected temperatures in Tables 4 and 5. Room-temperature data for end-member kieserite used throughout the present paper are given in Bechtold and Wildner (2016), and temperature-dependent data of $MgSO_4\cdot H_2O$ are found in Talla and Wildner (2019).

The structural behavior of the kieserite-dwornikite solid-solution series, $Mg_{1-x}Ni_xSO_4\cdot H_2O$, as derived from single-crystal X-ray diffraction measurements, is illustrated in Figures 2–4, and relevant crystal-chemical data of four selected representatives including the dwornikite end-member are given in Table 6. Additionally, Table 7 illustrates structural changes in the dwornikite end-member at low temperature. Respective details for end-member kieserite from Bechtold and Wildner (2016) are included for reference.

The kieserite structure type consists of kinked chains of O3(≡$H_2O$)-corner-sharing $MgO_4(H_2O)_2$ octahedra, clearly elongated along the octahedral water-water axis, with adjacent octahedra being further intra-linked by nearly regular $SO_4$ tetrahedra via common O2 corners. These octahedral-tetrahedral

**TABLE 3.** Structure parameters at room temperature for selected representatives of the $Mg_{1-x}Ni_x(SO_4)\cdot H_2O$ solid-solution series

| $Mg_{1-x}Ni_x(SO_4)\cdot H_2O$ | | $Mg_{0.76}Ni_{0.24}$ | $Mg_{0.48}Ni_{0.52}$ | $Mg_{0.24}Ni_{0.76}$ | $Mg_{0.00}Ni_{1.00}$ |
|---|---|---|---|---|---|
| Mg/Ni | $x_{Ni}$ | 0.236(2) | 0.525(2) | 0.759(2) | 1.0 |
| | $U_{11}$ | 85(2) | 69(1) | 67(1) | 57(1) |
| | $U_{22}$ | 92(2) | 86(1) | 74(1) | 69(1) |
| | $U_{33}$ | 103(2) | 84(1) | 72(1) | 62(1) |
| | $U_{23}$ | 4(1) | 3(1) | 3(1) | 2(1) |
| | $U_{13}$ | 37(2) | 29(1) | 31(1) | 25(1) |
| | $U_{12}$ | –4(2) | –3(1) | –3(1) | –3(1) |
| | $U_{eq}$ | 96(1) | 82(1) | 76(1) | 64(1) |
| S | $y$ | 0.15535(6) | 0.15612(3) | 0.15643(3) | 0.15664(4) |
| | $U_{11}$ | 71(2) | 56(1) | 53(1) | 44(1) |
| | $U_{22}$ | 89(2) | 76(1) | 62(1) | 59(1) |
| | $U_{33}$ | 111(2) | 92(1) | 77(1) | 67(1) |
| | $U_{13}$ | 36(1) | 26(1) | 28(1) | 23(1) |
| | $U_{eq}$ | 93(1) | 78(1) | 65(1) | 58(1) |
| O1 | $x$ | 0.17513(17) | 0.17421(10) | 0.17356(10) | 0.17289(12) |
| | $y$ | 0.04528(15) | 0.04590(10) | 0.04637 (9) | 0.04649(11) |
| | $z$ | 0.39678(17) | 0.39953(10) | 0.40142(10) | 0.40331(12) |
| | $U_{11}$ | 100(4) | 82(2) | 78(2) | 71(2) |
| | $U_{22}$ | 165(4) | 160(3) | 150(2) | 142(3) |
| | $U_{33}$ | 178(5) | 164(3) | 150(2) | 136(3) |
| | $U_{23}$ | 67(4) | 68(2) | 70(2) | 69(2) |
| | $U_{13}$ | 51(3) | 42(2) | 43(2) | 38(2) |
| | $U_{12}$ | 40(3) | 37(2) | 37(2) | 37(2) |
| | $U_{eq}$ | 154(2) | 142(1) | 130(1) | 121(1) |
| O2 | $x$ | 0.09460(18) | 0.09821(10) | 0.10079(10) | 0.10307(12) |
| | $y$ | 0.26806(14) | 0.26909 (9) | 0.26961 (8) | 0.26994 (9) |
| | $z$ | 0.15065(17) | 0.15246(10) | 0.15372(10) | 0.15466(11) |
| | $U_{11}$ | 133(4) | 118(2) | 127(2) | 95(2) |
| | $U_{22}$ | 125(4) | 117(2) | 114(2) | 95(2) |
| | $U_{33}$ | 186(5) | 164(3) | 170(3) | 135(3) |
| | $U_{23}$ | 49(3) | 43(2) | 51(2) | 43(2) |
| | $U_{13}$ | 94(4) | 82(2) | 94(2) | 71(2) |
| | $U_{12}$ | 11(3) | 14(2) | 16(2) | 14(2) |
| | $U_{eq}$ | 140(2) | 127(1) | 113(1) | 101(1) |
| O3 | $y$ | 0.63411(21) | 0.63291(12) | 0.63209(11) | 0.63135(13) |
| | $U_{11}$ | 104(6) | 98(3) | 91(3) | 79(3) |
| | $U_{22}$ | 140(6) | 123(3) | 109(3) | 103(3) |
| | $U_{33}$ | 131(6) | 108(3) | 94(3) | 82(3) |
| | $U_{13}$ | 52(5) | 47(3) | 45(2) | 37(3) |
| | $U_{eq}$ | 126(3) | 110(1) | 97(1) | 88(1) |
| H | $x$ | 0.092(4) | 0.111(3) | 0.111(3) | 0.108(4) |
| | $y$ | 0.688(4) | 0.700(3) | 0.695(3) | 0.694(3) |
| | $z$ | 0.286(4) | 0.294(3) | 0.291(3) | 0.296(3) |
| | $U_{iso}$ | 262(68) | 334(50) | 196(40) | 201(50) |

*Notes:* $U_{ij}$ are given in pm². Wyckoff positions: Mg/Ni on 4*b* (sym $\bar{1}$): 0, ½, 0, etc.; S and O3 on 4*e* (sym 2): 0, *y*, ¼ etc. $U_{23} = U_{12} = 0$; O1, O2, and H on 8*f* (sym 1): *x*, *y*, *z*, etc. Respective data for end-member kieserite are given in Bechtold and Wildner (2016).

**TABLE 4.** Crystal data and details of selected temperature-dependent X-ray data collections and structure refinements for dwornikite, $Ni(SO_4)\cdot H_2O$

| $Ni(SO_4)\cdot H_2O$ | 0 °C | –80 °C | –160 °C |
|---|---|---|---|
| $a$ (Å) | 6.825(1) | 6.812(1) | 6.804(1) |
| $b$ (Å) | 7.607(1) | 7.612(1) | 7.618(1) |
| $c$ (Å) | 7.459(1) | 7.444(1) | 7.437(1) |
| β (°) | 117.72(1) | 117.63(1) | 117.58(1) |
| $V$ (Å³) | 342.79 | 341.98 | 341.66 |
| μ ($mm^{-1}$) | 6.14 | 6.16 | 6.16 |
| $D_{calc}$ ($g/cm^3$) | 3.348 | 3.356 | 3.359 |
| Frame scale factors (max, min) | 0.75, 0.64 | 0.75, 0.66 | 0.75, 0.66 |
| Total number of reflections | 11574 | 11491 | 11115 |
| Intensity data for unit cell | 8253 | 8457 | 8497 |
| Unique *hkl* values | 1064 | 1063 | 1061 |
| $R_i$ (%) | 2.40 | 2.32 | 2.35 |
| $F_o > 4\sigma(F_o)$ | 1031 | 1036 | 1034 |
| wR2 (for all $F_o^2$) (%) | 4.11 | 4.20 | 4.22 |
| weighting parameters *a*, *b*[a] | 0.021, 0.34 | 0.021, 0.47 | 0.021, 0.53 |
| R1 [for $F_o > 4\sigma(F_o)$] (%) | 1.54 | 1.60 | 1.61 |
| R1 (for all $F_o$) (%) | 1.62 | 1.67 | 1.66 |
| Goodness of fit | 1.127 | 1.118 | 1.123 |
| Extinction coefficient | 0.025(1) | 0.021(1) | 0.019(1) |
| $\Delta\rho_{max,min}$ ($e^- Å^{-3}$) | 0.67, –0.68 | 0.80, –0.72 | 0.82, –0.67 |

*Notes:* Common data: monoclinic, space group *C*2/*c* (no. 15), $Z = 4$; each 930 CCD frames measured; exposure time/frame 10 s; 40 variables. Respective temperature-dependent data for end-member kieserite are given in Talla and Wildner (2019), its room temperature data in Bechtold and Wildner (2016), and those for dwornikite in Table 2.

[a] $w = 1/[\sigma^2(F_o^2) + (a \times P)^2 + b \times P]$; $P = \{[\max \text{ of } (0 \text{ or } F_o^2)] + 2F_c^2\}/3$.

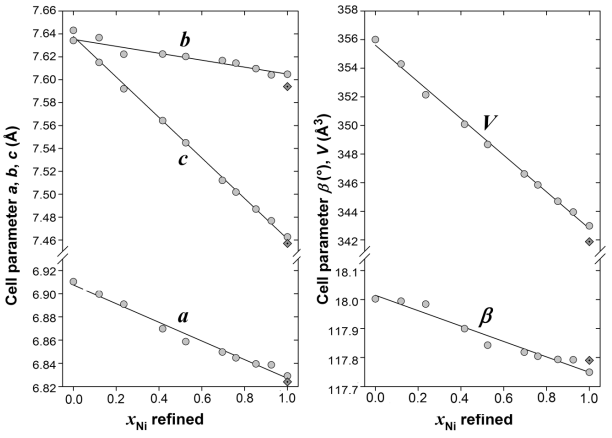


**FIGURE 2.** Variation of the lattice parameters (**a**) *a*, *b*, *c* and (**b**) β and *V* along the $Mg_{1-x}Ni_x(SO_4)\cdot H_2O$ solid-solution series with linear regression lines. Errors are equal or smaller than the symbol size. The data for end-member kieserite are taken from Bechtold and Wildner (2016). Previous data for dwornikite (Wildner and Giester 1991) are shown (without errors) as dotted diamond symbols.

chains are aligned parallel to the *c*-axis and interlinked to form a framework structure by sharing the polyhedral O1 corners as well as by moderately strong hydrogen bonds O3···O2.

The present X-ray measurements and structure refinements do not indicate any octahedral Mg-Ni cation ordering, domain formation, or related effects. Figure 2 shows the variation of the lattice parameters between kieserite and dwornikite. It is evident that complete miscibility exists and that the solid-solution series behaves according to Vegard's law (Vegard 1921), with all lattice parameters changing in a linear way across the entire series. The cell volume *V* (–13.0 Å³), angle β (–0.25°), and the lattice parameters *a*, *b*, and *c* (–0.08, –0.03, and –0.18 Å, respectively) all decrease with increasing Ni content. This is mainly driven by the clear decrease of the average metal-oxygen (Me–O) bond length and of the octahedral volume upon Ni intake, as shown in Figures 3a and 4a. The strongest reduction in individual bond lengths occurs for the Me–O3 bonds with the major vector component parallel to the *c*-axis, thus resulting in its strong decrease. The Me–O1 and Me–O2 bonds change much less, and Me–O1 even increases slightly (Fig. 3a, Table 6). Overall, the octahedral shape is preserved as a clear [4+2] coordination in dwornikite. In contrast to the octahedron, the tetrahedral $SO_4$ group slightly expands with increasing Ni-content, but tetrahedral bond length and also angular changes (Fig. 3d) rarely exceed a 3σ limit. The donor–acceptor distance of the medium-strength hydrogen bond O3–H···O2 shortens significantly at higher Ni contents (Fig. 4c).

Further factors contributing to the shrinkage of the unit cell with increasing Ni-content are polyhedral rotations and tiltings, evidenced by a significant decrease of the two Me–O–S angles shown in Figure 4b, whereas the chain angle Me–O3–Me mar-

**TABLE 5.** Selected temperature-dependent structure parameters for dwornikite, $Ni(SO_4)\cdot H_2O$

| $Ni(SO_4)\cdot H_2O$ | | 0 °C | −80 °C | −160 °C |
|---|---|---|---|---|
| Ni | $U_{11}$ | 52(1) | 39(1) | 27(1) |
| | $U_{22}$ | 63(1) | 47(1) | 32(1) |
| | $U_{33}$ | 55(1) | 41(1) | 28(1) |
| | $U_{23}$ | 2(1) | 2(1) | 1(1) |
| | $U_{13}$ | 22(1) | 17(1) | 13(1) |
| | $U_{12}$ | −2(1) | −1(1) | −1(1) |
| | $U_{eq}$ | 58(1) | 43(1) | 29(1) |
| S | *y* | 0.15681(3) | 0.15727(3) | 0.15763(4) |
| | $U_{11}$ | 40(1) | 31(1) | 23(1) |
| | $U_{22}$ | 54(1) | 42(1) | 30(1) |
| | $U_{33}$ | 60(1) | 45(1) | 32(1) |
| | $U_{13}$ | 20(1) | 16(1) | 12(1) |
| | $U_{eq}$ | 53(1) | 40(1) | 28(1) |
| O1 | *x* | 0.17279(10) | 0.17262(10) | 0.17257(10) |
| | *y* | 0.04668( 9) | 0.04732( 9) | 0.04772( 9) |
| | *z* | 0.40353(10) | 0.40413(10) | 0.40473( 9) |
| | $U_{11}$ | 65(2) | 52(2) | 39(2) |
| | $U_{22}$ | 132(3) | 100(2) | 70(2) |
| | $U_{33}$ | 125(2) | 94(2) | 67(2) |
| | $U_{23}$ | 63(2) | 46(2) | 32(2) |
| | $U_{13}$ | 36(2) | 28(2) | 20(2) |
| | $U_{12}$ | 32(2) | 25(2) | 18(2) |
| | $U_{eq}$ | 111(1) | 84(1) | 60(1) |
| O2 | *x* | 0.10339(10) | 0.10428(10) | 0.10507(10) |
| | *y* | 0.27006( 8) | 0.27059( 8) | 0.27108( 8) |
| | *z* | 0.15477( 9) | 0.15519( 9) | 0.15552( 9) |
| | $U_{11}$ | 89(2) | 67(2) | 51(2) |
| | $U_{22}$ | 86(2) | 66(2) | 47(2) |
| | $U_{33}$ | 122(2) | 94(2) | 67(2) |
| | $U_{23}$ | 38(2) | 26(2) | 18(2) |
| | $U_{13}$ | 66(2) | 51(2) | 38(2) |
| | $U_{12}$ | 12(2) | 7(2) | 3(2) |
| | $U_{eq}$ | 93(1) | 70(1) | 51(2) |
| O3 | *y* | 0.63108(12) | 0.63077(12) | 0.63055(12) |
| | $U_{11}$ | 76(3) | 60(3) | 42(3) |
| | $U_{22}$ | 92(3) | 70(3) | 56(3) |
| | $U_{33}$ | 76(3) | 61(3) | 50(3) |
| | $U_{13}$ | 37(2) | 29(2) | 22(2) |
| | $U_{eq}$ | 81(1) | 63(1) | 49(1) |
| H | *x* | 0.108(3) | 0.109(3) | 0.109(3) |
| | *y* | 0.695(2) | 0.695(3) | 0.695(3) |
| | *z* | 0.294(3) | 0.294(3) | 0.294(3) |
| | $U_{iso}$ | 197(43) | 204(48) | 200(50) |

*Notes:* $U_{ij}$ are given in $pm^2$. Wyckoff positions: Ni on 4*b* (sym $\bar{1}$): 0,½,0, etc.; S and O3 on 4*e* (sym 2): 0,*y*,¼, etc. $U_{23} = U_{12} = 0$; O1, O2, and H on 8*f* (sym 1): *x*,*y*,*z*, etc. Respective room-temperature data are given in Table 3.

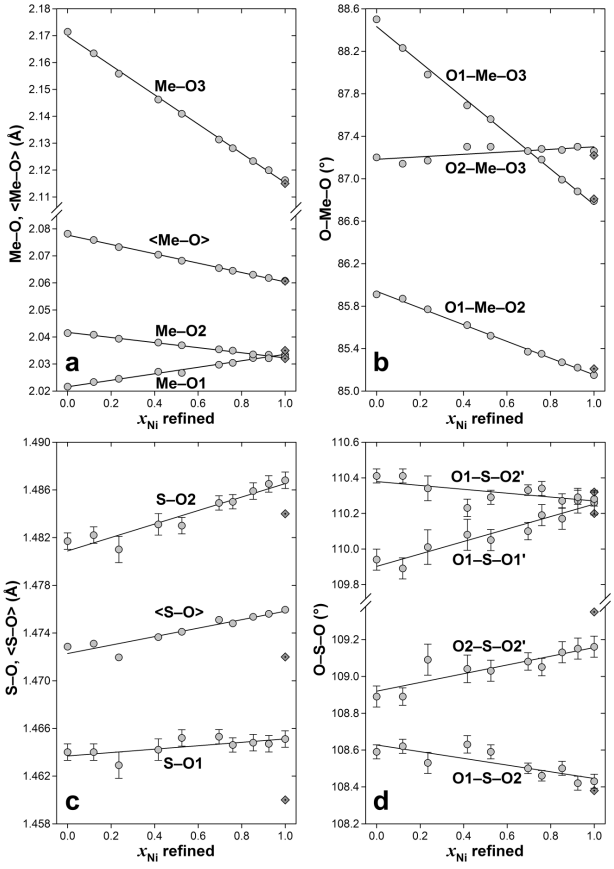


**FIGURE 3.** Polyhedral geometries along the $Mg_{1-x}Ni_x(SO_4)\cdot H_2O$ solid-solution series with linear regression lines; (**a**) octahedral Me–O bond lengths and (**b**) O–Me–O angles, (**c**) tetrahedral S–O bond lengths, and (**d**) O–S–O angles, where Me represents the metal cation. If not indicated, errors are equal or smaller than the symbol size. The data for end-member kieserite are taken from Bechtold and Wildner (2016). Previous data for dwornikite (Wildner and Giester 1991) are shown (without errors) as dotted diamond symbols.

ginally increases. As a consequence, the rigid $SO_4$ tetrahedron rotates by 3.2° around its twofold axis (also compare Fig. 5 in Talla and Wildner 2019).

As expected, when the temperature is reduced, the cell volume as well as β, *a*, and *c* decrease, but the *b* axis lengthens for dwornikite (Fig. 5), as also found for kieserite (Talla and Wildner 2019). Moreover, the mean Me–O bond lengths (Fig. 6a) and octahedral volumes (Fig. 5c) decrease, mainly by reducing the longest Me–O3 bond, and, thus, octahedral distortion is reduced, too. S–O bond lengths and the tetrahedral volume show an artificial increase upon cooling (Figs. 6d and 5c) due to changes in thermal motion: a "simple rigid bond" correction according to Downs et al. (1992) reveals practically constant <S–O> bond lengths within the full temperature range. The comparatively short O3–H···O2 hydrogen bond in dwornikite further shortens, but by only about half the extent compared to kieserite (Talla and Wildner 2019). A roughly analogous situation is also found for the polyhedra-linking Me–O–S angles in dwornikite that further decrease upon cooling, but less so than in kieserite (and szomolnokite; Talla and Wildner 2019).

## IR spectra

The IR spectra of $(Mg,Ni)SO_4\cdot H_2O$ feature several clearly discernible absorption features (Fig. 7). Additional weak absorptions related to OH and $H_2O$ combination modes are visible between 5200–4500 $cm^{-1}$ mainly in diffuse reflectance spectra of undiluted sample material (Fig. 8). In the FTIR spectra measured in transmission mode, the $H_2O$ absorption region is dominated by a prominent band at 3182–3057 $cm^{-1}$ (3.14–3.27 μm), representing the symmetric stretching vibration $\nu_{1(H_2O)}$ of the $H_2O$ molecule. A broad shoulder at higher wavenumbers (3367–3262 $cm^{-1}$/2.97–3.07 μm) represents $\nu_{3(H_2O)}$, the antisymmetric $H_2O$ stretching mode. The band positions of both $H_2O$ stretching vibrations decrease significantly in their wavenumber position upon Ni intake (Fig. 9a, Table 8), whereas the $H_2O$ bending vibration $\nu_{2(H_2O)}$ remains practically stable (1525–1522 $cm^{-1}$/6.56–6.57 μm). The same applies for the position of the strongest band in a major band group corresponding to the antisymmetric $\nu_{3(SO_4)}$ stretching mode of the sulfate tetrahedra (a band group centered at around 1150 $cm^{-1}$/8.70 μm) and the IR-

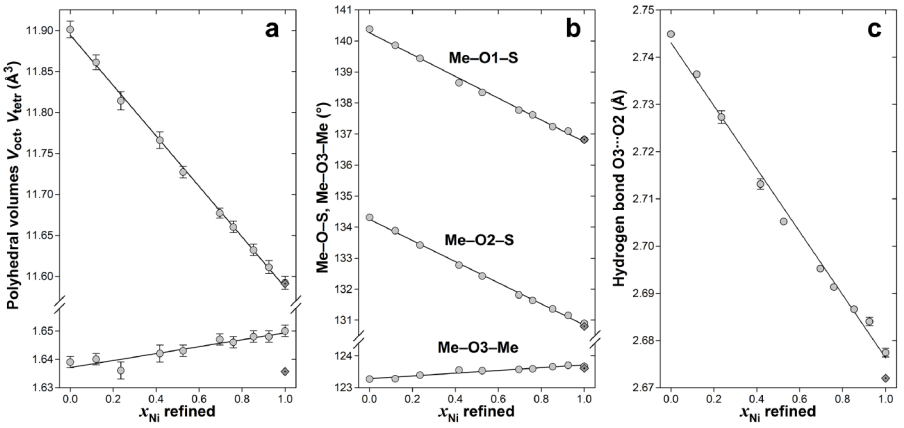


**FIGURE 4.** (**a**) Polyhedral volumes, (**b**) Me–O–S and Me–O–Me angles, and (**c**) hydrogen bond lengths along the $Mg_{1-x}Ni_x(SO_4)\cdot H_2O$ solid-solution series with linear regression lines. For **a**, note the very different scales for the tetrahedral and octahedral volumes. If not indicated, errors are equal or smaller than the symbol size. The data for end-member kieserite are taken from Bechtold and Wildner (2016). Previous data for dwornikite (Wildner and Giester 1991) are shown (without errors) as dotted diamond symbols.

**TABLE 6.** Survey of crystal-chemical data for selected representatives of the $Mg_{1-x}Ni_x(SO_4)\cdot H_2O$ solid-solution series: bond lengths (Å) and angles (°), polyhedral volumes (Å$^3$), bond strengths (without H atoms; calculated according to Brese and O'Keeffe 1991), and polyhedral distortion parameters (Brown and Shannon 1973; Robinson et al. 1971; Griffen and Ribbe 1979)

| $Mg_{1-x}Ni_x(SO_4)\cdot H_2O$ | $Mg_{1.00}Ni_{0.00}$ | $Mg_{0.76}Ni_{0.24}$ | $Mg_{0.48}Ni_{0.52}$ | $Mg_{0.24}Ni_{0.76}$ | $Mg_{0.00}Ni_{1.00}$ |
|---|---|---|---|---|---|
| $x_{Ni}$ | 0.0 | 0.236(2) | 0.525(2) | 0.759(2) | 1 |
| Me-O1 (2×) | 2.0216(7) | 2.0245(11) | 2.0267(7) | 2.0304(7) | 2.0334(8) |
| Me-O2 (2×) | 2.0414(7) | 2.0393(11) | 2.0370(7) | 2.0349(6) | 2.0327(7) |
| Me-O3 (2×) | 2.1714(6) | 2.1558(8) | 2.1409(5) | 2.1281(5) | 2.1162(5) |
| <Me-O> | 2.0782 | 2.0732 | 2.0682 | 2.0645 | 2.0608 |
| $\Delta_{oct}\times10^3$ | 1.023 | 0.802 | 0.622 | 0.476 | 0.362 |
| Σv.u. (Me) | 2.15 | 2.12 | 2.08 | 2.04 | 2.01 |
| | | | | | |
| O1-Me-O2 (2×)[a] | 85.91(3) | 85.77(5) | 85.52(3) | 85.35(3) | 85.15(3) |
| O1-Me-O3 (2×)[a] | 88.50(2) | 87.98(3) | 87.56(2) | 87.18(2) | 86.79(2) |
| O2-Me-O3 (2×)[a] | 87.20(3) | 87.17(5) | 87.30(3) | 87.28(3) | 87.26(2) |
| $\sigma^2_{oct}$ | 9.75 | 10.90 | 12.11 | 13.44 | 15.03 |
| $V_{oct}$ | 11.901(10) | 11.814(11) | 11.727(7) | 11.660(7) | 11.592(8) |
| S-O1 (2×) | 1.4639(7) | 1.4629(11) | 1.4652(7) | 1.4646(6) | 1.4651(7) |
| S-O2 (2×) | 1.4817(7) | 1.4810(11) | 1.4830(6) | 1.4850(6) | 1.4868(7) |
| <S-O> | 1.4728 | 1.4720 | 1.4741 | 1.4748 | 1.4760 |
| BLDP×10$^3$ | 6.98 | 7.10 | 6.99 | 7.99 | 8.49 |
| Σv.u. (S) | 6.02 | 6.03 | 6.00 | 5.99 | 5.97 |
| | | | | | |
| O1-S-O1′ | 109.94(6) | 110.01(9) | 110.05(6) | 110.19(6) | 110.26(7) |
| O1-S-O2 (2×) | 108.59(4) | 108.53(6) | 108.59(4) | 108.46(3) | 108.43(4) |
| O1-S-O2′(2×) | 110.41(4) | 110.34(7) | 110.29(4) | 110.34(4) | 110.28(4) |
| O2-S-O2′ | 108.89(6) | 109.09(9) | 109.03(6) | 109.05(5) | 109.16(6) |
| $\sigma^2_{tetr}$ | 0.77 | 0.74 | 0.68 | 0.85 | 0.84 |
| $V_{tetr}$ | 1.639(2) | 1.636(3) | 1.643(2) | 1.646(2) | 1.650(2) |
| | | | | | |
| Me-O1-S | 140.38(4) | 139.44(7) | 138.34(4) | 137.62(4) | 136.82(5) |
| Me-O2-S | 134.31(4) | 133.42(7) | 132.42(4) | 131.63(4) | 130.89(4) |
| Me-O3-Me | 123.27(5) | 123.39(7) | 123.53(4) | 123.59(4) | 123.67(5) |
| Σv.u. (O1) | 1.95 | 1.94 | 1.92 | 1.91 | 1.90 |
| Σv.u. (O2) | 1.86 | 1.85 | 1.84 | 1.82 | 1.81 |
| Σv.u. (O3) | 0.55 | 0.56 | 0.56 | 0.57 | 0.57 |
| O3···O2 | 2.7449(8) | 2.7273(13) | 2.7052(8) | 2.6913(8) | 2.6774(9) |
| O3-H | 0.81(2) | 0.69(3) | 0.84(2) | 0.83(2) | 0.81(2) |
| O2···H | 2.01(2) | 2.07(3) | 1.92(2) | 1.90(2) | 1.92(2) |
| O3-H···O2 | 151(2) | 158(3) | 155(2) | 159(2) | 156(2) |

*Note:* Data for end-member kieserite are reproduced from Bechtold and Wildner (2016).
[a] Plus corresponding obtuse angles.

**TABLE 7.** Survey of selected temperature-dependent crystal-chemical data for dwornikite, $Ni(SO_4)\cdot H_2O$: bond lengths (Å) and angles (°), polyhedral volumes (Å$^3$), bond strengths (without H atoms, calculated according to Brese and O'Keeffe 1991), and polyhedral distortion parameters (Brown and Shannon 1973; Robinson et al. 1971; Griffen and Ribbe 1979)

| $Ni(SO_4)\cdot H_2O$ | 0 °C | −80 °C | −160 °C |
|---|---|---|---|
| Ni-O1 (2×) | 2.0338(7) | 2.0336(7) | 2.0336(7) |
| Ni-O2 (2×) | 2.0328(6) | 2.0317(6) | 2.0309(6) |
| Ni-O3 (2×) | 2.1145(5) | 2.1106(5) | 2.1085(5) |
| <Ni-O> | 2.0604 | 2.0586 | 2.0577 |
| $\Delta_{oct}\times10^3$ | 0.345 | 0.319 | 0.305 |
| Σv.u. (Ni) | 2.01 | 2.02 | 2.02 |
| | | | |
| O1-Ni-O2 (2×)[a] | 85.15(3) | 85.15(3) | 85.13(3) |
| O1-Ni-O3 (2×)[a] | 86.78(2) | 86.82(2) | 86.81(2) |
| O2-Ni-O3 (2×)[a] | 87.28(3) | 87.31(3) | 87.33(3) |
| $\sigma^2_{oct}$ | 15.01 | 14.86 | 14.92 |
| $V_{oct}$ | 11.585(7) | 11.557(7) | 11.540(7) |
| S-O1 (2×) | 1.4654(6) | 1.4657(7) | 1.4672(7) |
| S-O2 (2×) | 1.4869(6) | 1.4872(6) | 1.4888(6) |
| <S-O> | 1.47615 | 1.47645 | 1.4780 |
| BLDP×10$^3$ | 8.41 | 8.41 | 8.44 |
| Σv.u. (S) | 5.97 | 5.96 | 5.94 |
| | | | |
| O1-S-O1′ | 110.26(6) | 110.36(6) | 110.41(6) |
| O1-S-O2 (2×) | 108.44(3) | 108.45(4) | 108.46(4) |
| O1-S-O2′ (2×) | 110.25(4) | 110.24(4) | 110.23(4) |
| O2-S-O2′ | 109.19(5) | 109.10(5) | 109.04(5) |
| $\sigma^2_{tetr}$ | 0.81 | 0.84 | 0.85 |
| $V_{tetr}$ | 1.650(2) | 1.651(2) | 1.657(2) |
| | | | |
| Ni-O1-S | 136.75(4) | 136.63(4) | 136.47(4) |
| Ni-O2-S | 130.79(4) | 130.57(4) | 130.38(4) |
| Ni-O3-S | 123.73(4) | 123.72(4) | 123.72(4) |
| Σv.u. (O1) | 1.89 | 1.89 | 1.89 |
| Σv.u. (O2) | 1.81 | 1.81 | 1.80 |
| Σv.u. (O3) | 0.58 | 0.58 | 0.59 |
| O3···O2 | 2.6760(8) | 2.6706(8) | 2.6667(8) |
| O3-H | 0.81(2) | 0.82(2) | 0.82(2) |
| O2···H | 1.91(2) | 1.90(2) | 1.89(2) |
| O3-H···O2 | 156 (2) | 157(2) | 157(2) |

*Notes:* Respective room-temperature data are given in Table 6, those for end-member kieserite in Bechtold and Wildner (2016); temperature-dependent data for kieserite are given in Talla and Wildner (2019).
[a] Plus corresponding obtuse angles.

forbidden symmetric stretching mode $\nu_{1(SO_4)}$, visible as a weak but well-defined band at around 1030 cm$^{-1}$ (9.71 μm). A pronounced absorption phenomenon, even considered as a potential diagnostic feature for kieserite-group compounds by Lane (2007) and Lane et al. (2015), henceforth labeled "Peak 900 cm$^{-1}$", occurs at wavenumbers from 884 to 941 cm$^{-1}$ (11.31–10.63 μm) with increasing Ni content. Last, a band group at 630 cm$^{-1}$ (15.87 μm) is assigned to the tetrahedral $\nu_{4(SO_4)}$ bending modes.

It must be noted that the absorption band shape and even position vary between individual FTIR measuring modes (Fig. 7, Table 8). As example, the symmetric stretching vibration of the $H_2O$ molecule occurs at 3182 cm$^{-1}$ in kieserite measured in transmission mode, whereas it is centered at 3165 cm$^{-1}$ in ATR mode and as high as 3203 cm$^{-1}$ using the DRIFT technique on the

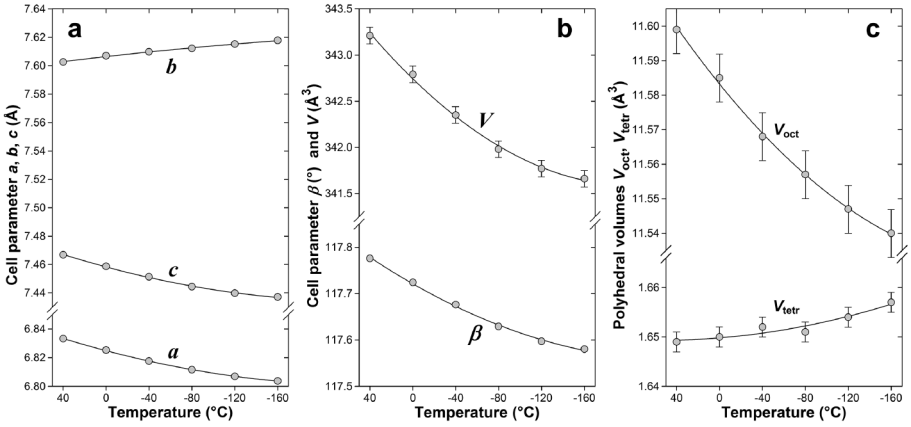


**Figure 5.** Variation of the lattice parameters (**a**) *a*, *b*, *c* and (**b**) β and *V*, as well as (**c**) polyhedral volumes ($V_{tetr}$ not corrected for thermal motion) for dwornikite within the investigated temperature range, with second-order regression lines. If not indicated, errors are equal or smaller than the symbol size. For **c**, note the somewhat different scales for the tetrahedral and octahedral volumes.

very same sample. Nevertheless, the overall spectral appearance is comparable, with the absorptions related to the $H_2O$ bending vibration and the $H_2O$ combination modes being enhanced in DRIFT spectra (Figs. 7 and 8, respectively), especially on pure sample material. Contrary to this specific benefit of using undiluted material, significant features such as the "Reststrahlen band" (labeled "R" in Fig. 7), a pronounced absorption at around 1300 $cm^{-1}$, obscure the expected intrinsic sulfate vibrations between 1300 and 370 $cm^{-1}$. The spectral position of these features, however, is also dependent on the sample composition, e.g., the Reststrahlen band decreases in position from 1360 to 1286 $cm^{-1}$ (7.35–7.77 μm) between kieserite and dwornikite.

The enhanced amplitude of absorption bands assigned to $H_2O$ combination modes in the 4400–5200 $cm^{-1}$ (2.27–1.92 μm) spectral region in diffuse reflectance spectra of undiluted sample material allows for their meaningful evaluation. Three distinct bands occur in this region at 4688, 4845, and 5087 $cm^{-1}$ (2.13, 2.06, and 1.97 μm, respectively) in kieserite. As the Ni content increases, both peripheral bands diverge from the original central band position for kieserite at 4845 $cm^{-1}$ to 4566 and 5110 $cm^{-1}$ (2.19 and 1.96 μm, respectively), thus enhancing the band separation with increasing Ni (Figs. 8a and 8b), while the central band

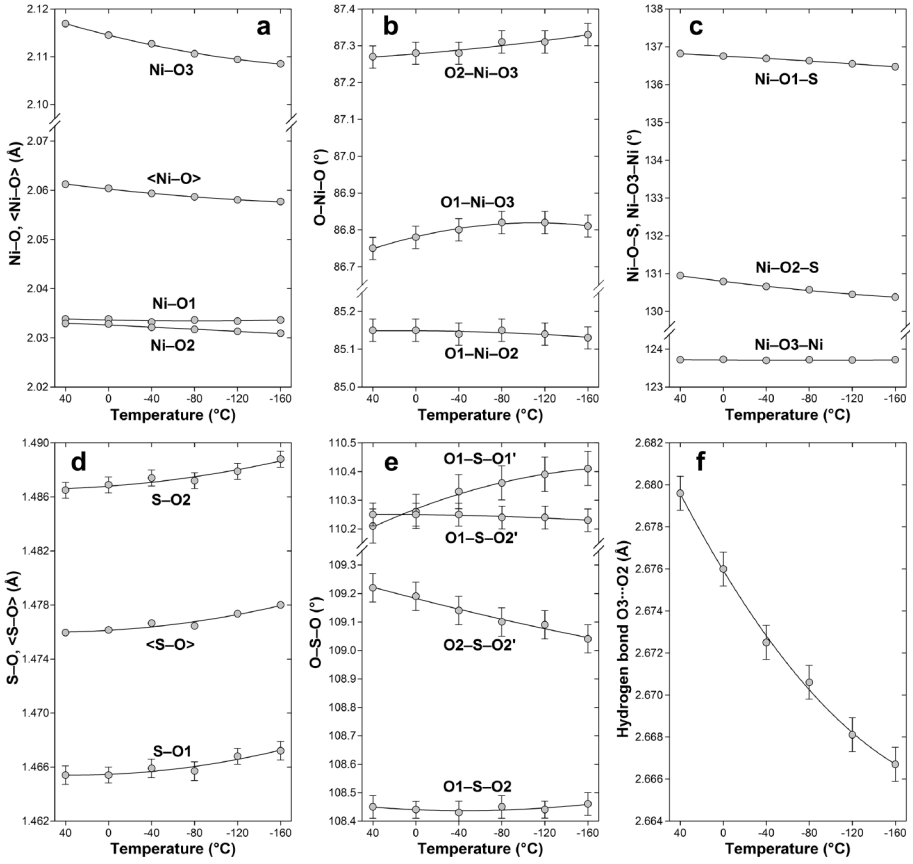


**Figure 6.** Variation of the polyhedral geometries (**a**) octahedral Me–O bond lengths and (**b**) O–Me–O angles, (**d**) tetrahedral S–O bond lengths (uncorrected for thermal motion) and (**e**) O–S–O angles, as well as of (**c**) Ni–O–S and Ni–O–Ni angles and (**f**) the hydrogen bond length in dwornikite within the investigated temperature range, with second-order regression lines. If not indicated, errors are equal or smaller than the symbol size.

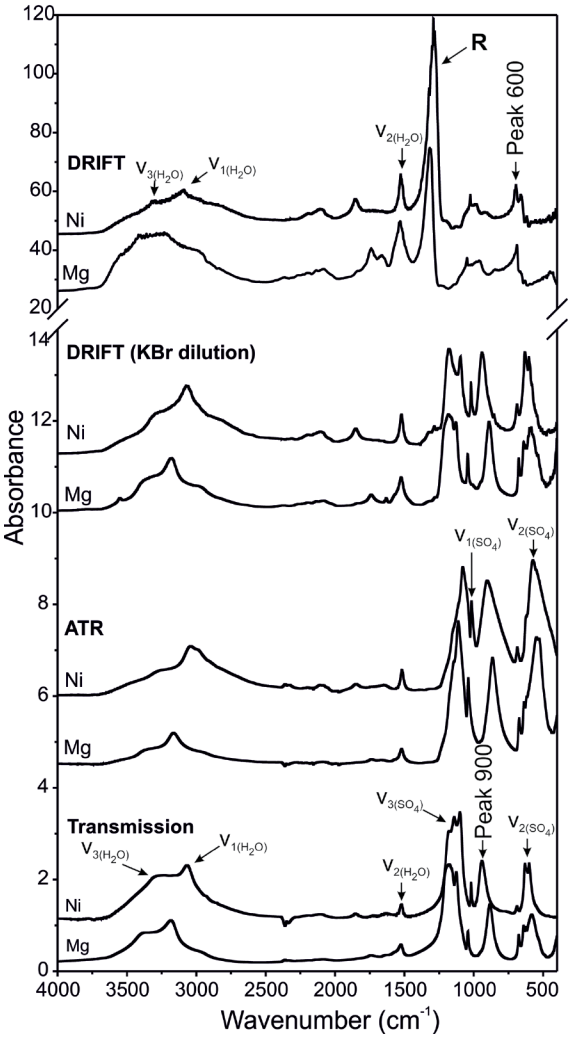


**Figure 7.** FTIR spectra of kieserite (Mg) and dwornikite (Ni) in each measuring mode. In addition to band position changes between the end-members, note the differences in band positions and shapes between the various measuring modes. Data for kieserite are taken from Talla and Wildner (2019).

itself shifts down to 4735 $cm^{-1}$ (2.11 μm).

In many cases, the observed changes in spectral band position are limited, such as for the sulfate vibrations with ≤30 $cm^{-1}$ in all three measuring modes, and that of the $H_2O$ bending mode, with a minimal decrease of only 3 $cm^{-1}$ from kieserite to the dwornikite end-member.

Pronounced linear correlation trends can be observed for the $H_2O$ stretching vibrations, where the well-resolved $\nu_{1(H_2O)}$ band changes in position from 3182 to 3057 $cm^{-1}$ and the $\nu_{3(H_2O)}$ shoulder decreases in wavenumber from 3367 to 3262 $cm^{-1}$ between kieserite and dwornikite. A somewhat smaller but still prominent linear change can be seen for the apparent kieserite-group "diagnostic" absorption band (Lane 2007; Lane et al. 2015), increasing from 884 in kieserite to 941 $cm^{-1}$ with increasing Ni content (Fig. 9a).

The variation in the wavenumber position of the relevant spectral absorption phenomena in the scope of the individual measurement modes, as well as the respective linear regression coefficients are summarized in Table 8.

The results of FTIR measurements at low temperature, depicted for the Mg-Ni solid-solution series in Figure 10a, show significant changes in the wavenumber position of the $H_2O$ stretching vibrations, which decrease significantly upon cooling. On the contrary, the "diagnostic" band at ~900 $cm^{-1}$ increases in wavenumber. The vibrations of the sulfate tetrahedra remain nearly unaffected throughout the entire temperature range, as is also true for the $H_2O$ bending vibration. Reduced fitting accuracy obscures any observable temperature-related trend for the $\nu_{3(H_2O)}$ band (Fig. 10a).

### Raman spectra

The Raman spectra consist of numerous narrow bands in the 100–1600 $cm^{-1}$ shift region, with much better resolution compared to FTIR spectra (Fig. 9 vs. 11a). The most prominent band is the symmetric stretching vibration $\nu_{1(SO_4)}$ of the sulfate tetrahedron at 1042 and 1020 $cm^{-1}$ shift in kieserite and dwornikite, respectively. Several relevant spectral features occur at lower shift values, the most prominent situated at ~220, ~430, and a doublet at ~630 $cm^{-1}$ shift. Weak bands occur in the 1100–1600 $cm^{-1}$ spectral region. With the excep-

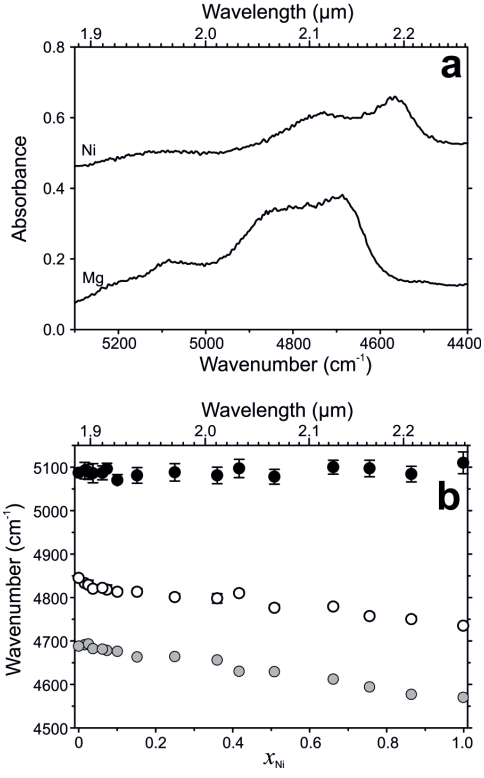


**Figure 8.** Spectral region with three diagnostic $H_2O$ combination modes, (**a**) observed in DRIFT measurements of kieserite (from Talla and Wildner 2019) and dwornikite on undiluted sample material, (**b**) detailed plot of band position change for the examined bands across the kieserite-dwornikite solid-solution series. Errors equal or smaller than the symbol size are not plotted.

**TABLE 8.** Wavenumber positions of relevant absorption phenomena in FTIR spectra in each measuring mode for the kieserite and dwornikite end-members, Mg/Ni($SO_4$)·$H_2O$, at room temperature

| Vibration | Wavenumber position ($cm^{-1}$) | | Linear regression coefficients[a] | |
|---|---|---|---|---|
| | Kieserite | Dwornikite | a | b |
| **Transmission (1:300 sample dilution in KBr)** | | | | |
| Peak 900 | 884(1) | 941(2) | 52(3) | 887(1) |
| $n_{1(SO_4)}$ | 1043(1) | 1019(1) | −26(2) | 1041(1) |
| $n_{3(SO_4)center}$ | 1165(1) | 1135(1) | −24(3) | 1164(1) |
| $n_{2(H_2O)}$ | 1525(4) | 1522(2) | −4(1) | 1526(1) |
| $n_{1(H_2O)}$ | 3182(4) | 3057(5) | −134(7) | 3191(3) |
| $n_{3(H_2O)}$ | 3367(12) | 3262(21) | −117(12) | 3364(5) |
| **Attenuated Total Reflectance (ATR)** | | | | |
| Peak 900 | 866(3) | 904(6) | 35(4) | 860(2) |
| $n_{2(H_2O)}$ | 1520(1) | 1517(2) | −3(4) | 1520(1) |
| $n_{1(H_2O)}$ | 3165(4) | 3037(5) | −127(3) | 3163(1) |
| $n_{3(H_2O)}$ | 3345(8) | 3292(22) | −37(6) | 3347(3) |
| **Diffuse reflectance (1:20 sample dilution in KBr)** | | | | |
| Peak 900 | 886(3) | 938(2) | 53(2) | 890.6(8) |
| $n_{1(SO_4)}$ | 1044(2) | 1020(1) | −26.6(9) | 1044(1) |
| $n_{3(SO_4)center}$ | 1172(3) | 1143(4) | −24(3) | 1166(2) |
| $n_{2(H_2O)}$ | 1523(1) | 1521(1) | 2.8(4) | 1523(1) |
| $n_{1(H_2O)}$ | 3180(2) | 3062(8) | −121(5) | 3188(3) |
| $n_{3(H_2O)}$ | 3365(13) | 3265(20) | −88(5) | 3353(3) |
| **Diffuse reflectance (non-diluted sample)** | | | | |
| Peak 600 | 690(1) | 696(2) | 8(1) | 687.4(6) |
| Reststrahlenband | 1316(6) | 1286(3) | −31(4) | 1310(2) |
| $n_{2(H_2O)}$ | 1526(3) | 1525(1) | −1.4(9) | 1527(1) |
| $n_{1(H_2O)}$ | 3203(20) | 3099(6) | −107(4) | 3207(2) |
| $n_{3(H_2O)}$ | 3412(23) | 3314(19) | −129(48) | 3432(22) |
| Peak 4700 $cm^{-1}$ | 4688(4) | 4566(4) | −123(4) | 4690(2) |
| Peak 4850 $cm^{-1}$ | 4845(3) | 4735(5) | −92(6) | 4830(3) |
| Peak 5090 $cm^{-1}$ | 5087(10) | 5110(25) | 13(7) | 5085(3) |

*Notes:* Linear regression coefficients of the correlation between the wavenumber position of each absorption feature and the Ni-content ($x_{Ni}$) are listed. Positions of weak yet important bands observed in the region of $H_2O$ combination modes are given in the scope of DRIFT measurements on undiluted sample material.
[a] Linear regression equation $y = \mathbf{a}(x_{Ni}) + \mathbf{b}$, where $y$ denotes the wavenumber position of the vibration mode.

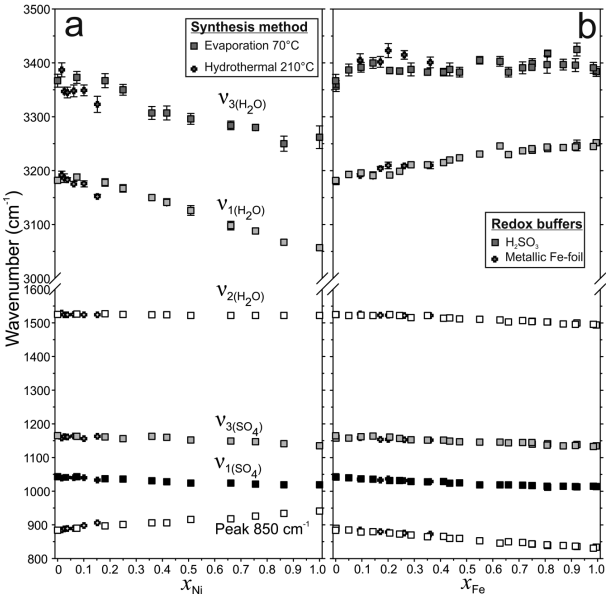


**FIGURE 9.** Dependence of the positions of relevant FTIR absorption features (transmission measurements) of the $Mg_{1-x}Me_x(SO_4)·H_2O$ solid solutions (**a**) on the Ni-content and (**b**) on the Fe-content at room temperature (RT). Data for the Mg-Fe solid solution are taken from Talla and Wildner (2019). Note the opposite trends in the $H_2O$-related modes. Errors equal or smaller than the symbol size are not plotted.

tion of the somewhat broader peak at roughly 1500 $cm^{-1}$ ($H_2O$ bending vibration), these bands are assigned to the split $\nu_{3(SO_4)}$ vibration (Stoilova and Lutz 1998; Chio et al. 2007). Stretching vibrations of the $H_2O$ molecule are visible in the expected spectral region with the antisymmetric $\nu_{3(H_2O)}$ contribution present as a mere poorly defined shoulder of the $\nu_{1(H_2O)}$ band, which decreases from 3179 down to 3071 $cm^{-1}$ with increasing Ni-content (Fig. 12a, Table 9). The position of the $H_2O$ bending mode remains constant in analogy to FTIR results, while most sulfate-related bands show a slight decrease upon Ni uptake with the exception of the two peaks assigned to the $\nu_{2(SO_4)}$ bending mode in the ~400–500 $cm^{-1}$ shift spectral region (Fig. 12a). The position of the band at ~220 $cm^{-1}$ shift assigned by Chio et al. (2007) to a translational mode of $H_2O$ and the $MeO_6$ octahedra increases significantly upon Ni uptake, as is also observed for the band assigned to "lattice modes" at ~120 $cm^{-1}$ shift.

Linear changes in band position can also be seen in the Raman spectra acquired across the (Mg,Ni)$SO_4·H_2O$ solid solution, as could be expected from the FTIR results (Table 9). Figure 12a illustrates the situation in detail, while Table 9 gives the respective coefficients of the linear regression between the band position and $x_{Ni}$.

Raman measurements at low temperature show a significant temperature dependence of the spectral position of certain modes, in analogy to the results of low-temperature FTIR measurements. The very good resolution and low FWHM of the bands in Raman spectra allow us to accurately examine even the subtle positional changes of sulfate modes, which are not so apparent in IR spectra (Table 9). In some cases, unfortunately, the amplitude of some of the monitored Raman bands is largely suppressed due to an unfavorable respective crystal orientation, causing increased errors upon fitting.

Despite this, a composition-independent systematic shift of the band position with temperature is seen mainly for the $\nu_{1(H_2O)}$ band, which decreases in wavenumber by about 30 $cm^{-1}$ across the full temperature range from +40 to –196 °C, and represents the strongest observable change among all examined bands. As a shoulder of the well-defined $\nu_{1(H_2O)}$ band, the $\nu_{3(H_2O)}$ band is generally poorly resolved, thus impeding any precise fit. The wavenumber change with temperature for bands related to sulfate vibrations is, as seen also in FTIR spectra, quite small, in general never exceeding 10 $cm^{-1}$ in the examined temperature range (Table 9). A systematic increase in wavenumber is observed at low temperature for the lowest-energetic bands, representing Mg(Ni)–O stretching modes according to Chio et al. (2007). For all observed bands, the rates at which the band positions change with temperature remain constant across the entire examined temperature range, allowing to determine a mean shift value per 1 °C for the individual bands, included in Table 9.

### UV-Vis-NIR spectroscopy and crystal field calculations

The optical absorption spectrum of dwornikite is shown in Figure 13. Three intense crystal field absorption bands are

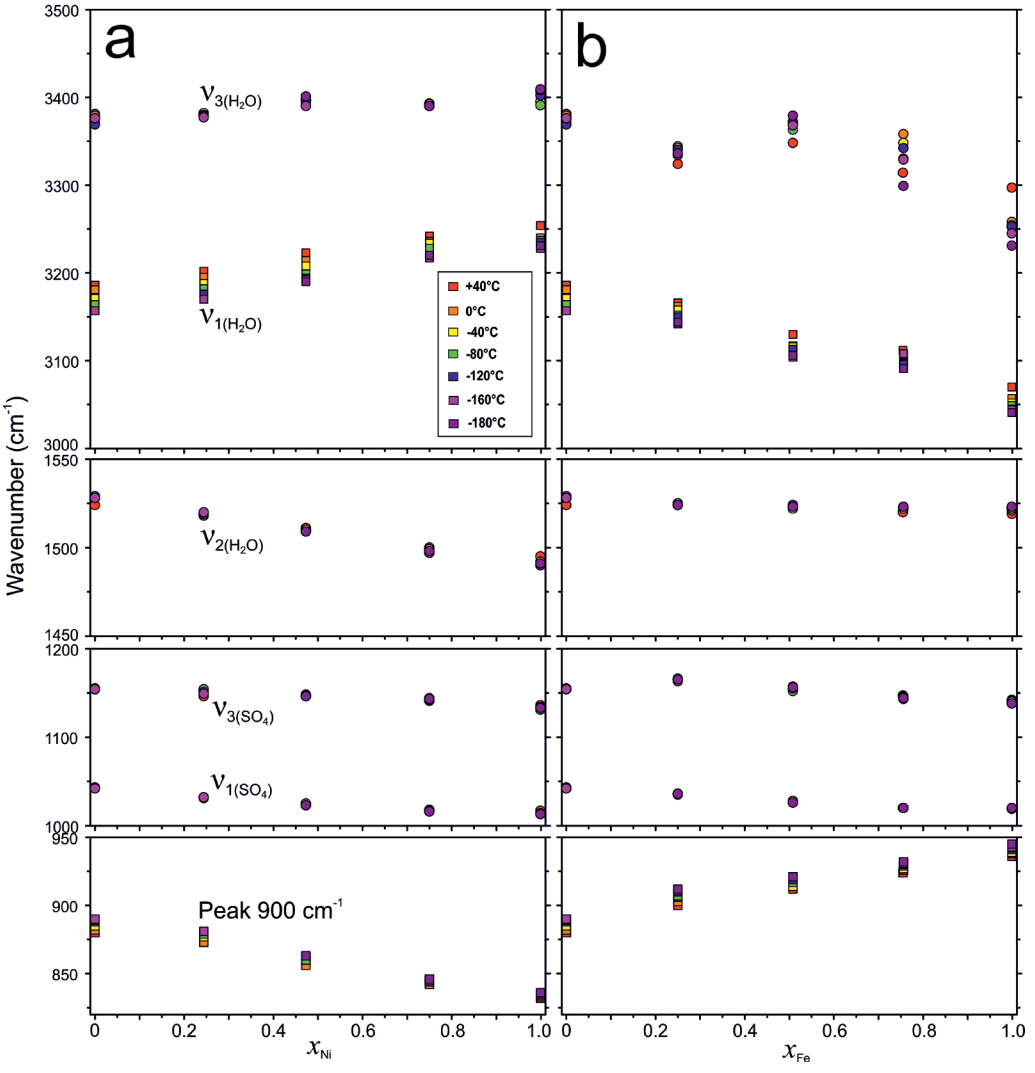


**Figure 10.** Dependence of the FTIR absorption band positions of (**a**) the $Mg_{1-x}Ni_x(SO_4)\cdot H_2O$ solid solution and (**b**) the $Mg_{1-x}Fe_x(SO_4)\cdot H_2O$ on temperature, as seen in transmission mode. Data for the Mg-Fe solid solution are taken from Talla and Wildner (2019). (Color online.)

observed around 8100, 13 450, and 24 600 cm$^{-1}$, which are assigned to spin-allowed electronic transitions from the $^3A_{2g}(F)$ ground state to the $^3T_{2g}(F)$, $^3T_{1g}(F)$, and $^3T_{1g}(P)$ levels of $Ni^{2+}$ ($3d^8$ electron configuration) in octahedral ($O_h$) symmetry. The latter two bands are modified by spin-forbidden states, i.e., $^1E_g(D)$ within the high-wavenumber slope of the mid-energy band, and $^1T_{2g}(D)$ near the onset of the high-energy band; the structures below 6600 cm$^{-1}$ originate from vibrational combination and overtone modes of the $H_2O$ molecule. Evidently, no significant splitting of the first and third spin-allowed bands is observed, either by the naked eye or via peak-fitting analyses, as would be expected from the geometric [4+2] elongation of the $NiO_6$ octahedron (Table 6, Fig. 3a). A splitting might be postulated for the middle spin-allowed band (with the main component at 13 450 cm$^{-1}$), but due to spin-orbit mixing and intensity stealing by the spin-forbidden $^1E_g(D)$ level, the position and intensity contribution of this second split component of $^3T_{1g}(F)$ can only be roughly estimated (~14 800 cm$^{-1}$). The refined crystal field and interelectronic repulsion parameters resulting from these assignments are summarized in Table 10, and respective observed and calculated energy levels (from the "classical" tetragonal CF approach) are included in Figure 13.

## Discussion

### Crystal-structural evolution and crystal chemistry

The present crystal-structure investigations corroborate the existence of a continuous solid-solution series, $Mg_{1-x}Ni_xSO_4\cdot H_2O$, between kieserite, $MgSO_4\cdot H_2O$, and isotypic dwornikite, $NiSO_4\cdot H_2O$. In view of previous crystal structure investigations of the two end-members (for kieserite: Bechtold and Wildner 2016; Hawthorne et al. 1987; for dwornikite: Wildner and Giester 1991), the respective solid-solution series behaves according to "basic" expectations. In particular, all lattice parameters

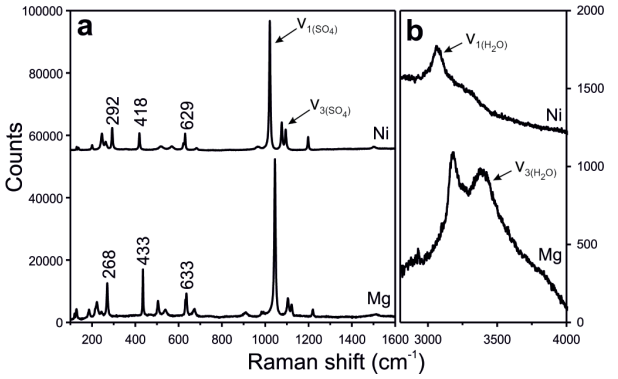


**Figure 11.** Raman spectra of dwornikite (Ni) and kieserite (Mg) at room temperature in the region of (**a**) tetrahedral, octahedral, and lattice modes, and (**b**) in the region of the O–H stretching modes. Data for kieserite are taken from Talla and Wildner (2019).

and crystal-chemical data exhibit Vegard-type behavior within the limits of error, undergoing linear changes with increasing Mg/Ni ratio. This trend serves as basis for any further theoretical calculations of interest, and the significant linear changes between the end-members importantly allow, among others, to infer the Mg/Ni ratio in binary kieserite-group samples of unknown composition from X-ray data. Vegard-type behavior indicates one-site ideal mixing of the end-members (Powell and Holland 1993), as is also the case with the recently investigated kieserite-szomolnokite solid solution (Talla and Wildner 2019). Enthalpy, entropy, molar volume, as well as heat capacity and thermal expansion can be determined by the linear combination of these parameters for both end-members in their respective formula ratio in the sample (van Hinsberg et al. 2005a, 2005b).

Likewise, the crystal-chemical expectations are fulfilled in the sense that the replacement of the larger Mg cation ($r_{Mg}$ = 0.720 Å) by the smaller $Ni^{2+}$ ($r^{2+}_{Ni}$ = 0.690 Å; all radii from Shannon 1976) leads to a decrease of the Me–O2 and especially Me–O3 bond lengths as well as of the average <Me–O> distance, and consequently to a reduction of the respective octahedral and the unit-cell volume (Figs. 2b, 3a, and 4a). Due to a slight increase of the Me–O1 bonds with Ni-content, a characteristic [4+2] coordination of the $MeO_6$ polyhedron is also realized in dwornikite (as in kieserite and most other kieserite-group sulfates, e.g., cobaltkieserite; Bechtold and Wildner 2016) rather than tending toward a [2+2+2]-type coordination, such as for the $FeO_6$ polyhedron in szomolnokite (Talla and Wildner 2019). In the latter case of the Mg-Fe solid solution ($r^{2+}_{Fe}$ = 0.780 Å), the cell parameters (except for the *b*-axis) and all Me–O bond lengths significantly increase with Fe content.

In contrast to the octahedron, the tetrahedral $SO_4$ group very slightly expands with increasing Ni-content (Figs. 3c and 4a), a behavior analogously observed in the respective Mg-Fe and Mg-Co solid solutions (Talla and Wildner 2019; Bechtold and Wildner 2016). The donor–acceptor distance of the medium-strength hydrogen bond O3–H···O2 shortens significantly at higher Ni contents (Fig. 4c), with an important impact on the vibrational spectra discussed below.

The unit-cell contraction is not only driven by the reduction of the Ni–O compared to the Mg–O bond lengths (Fig. 3a), but further intensified by octahedral-tetrahedral tiltings via reduced Me–O–S angles with increasing $x_{Ni}$ (Fig. 4b), meaning that the contraction exceeds the one expected from the mere differences in the $Me^{2+}$ ionic radii. This finding parallels those observed for the kieserite-cobaltkieserite (Bechtold and Wildner 2016) and kieserite-szomolnokite (Talla and Wildner 2019) solid solutions. It has been attributed by those authors to the absence (in case of Mg) vs. the presence of 3*d* orbitals (as for Co, Fe, and Ni); hence, for detailed discussions on this subject, which fully applies to the present case of the replacement of Mg by Ni, the reader is referred to those papers (and references therein). Similarly, the apparent difference in the character of the octahedral bond length distortion, i.e., a clear [4+2]-type elongation in kieserite, dwornikite, and all other kieserite-group end-member compounds except szomolnokite, which displays a tendency toward a [2+2+2] distortion, has been amply addressed by Talla and Wildner (2019), linking it with the 3*d*-electron configuration of the particular $Me^{2+}$ cation.

## IR, Raman, and crystal field spectra

**IR spectra at ambient conditions.** The linear Vegard-type behavior observed in the structural data for the $Mg_{1-x}Ni_xSO_4 \cdot H_2O$ solid-solution series (Figs. 2–4) is also reflected in the results of FTIR and Raman spectroscopic measurements. With wavenumber units in use, linear shifts of the IR spectral bands positions across the kieserite-dwornikite solid-solution series (Fig. 9a, Table 8) are recognized, in principle allowing to deduce the respective Mg/Ni ratio solely from spectroscopic data.

The evidence that the wavenumbers of both stretching modes of the $H_2O$ molecule, $\nu_{1(H_2O)}$ and $\nu_{3(H_2O)}$, decrease upon Ni uptake is in agreement with the single-crystal X-ray results (Fig. 4c, Table 6), where a decrease in the hydrogen bond length between the O3 donor and the O2 acceptor oxygen with increasing $x_{Ni}$ can be correlated with the observed band behavior according to well-established trends (Libowitzky 1999). The opposite behavior occurs in the kieserite-szomolnokite solid solution, where Fe contents lead to the lengthening of the O3···O2 donor-acceptor distance, resulting in an increase in wavenumber observable mainly for the $\nu_{1(H_2O)}$ stretching mode (Talla and Wildner 2019, Fig. 9b). The more or less constant position of the bending vibration of the $H_2O$ molecule independent of the Ni content indicates a rigid character of the $H_2O$ molecule, despite the widening of the acceptor–donor–acceptor angle O2–O3–O2 from kieserite to dwornikite (136.7–140.5°). Both the symmetric $\nu_{1(SO_4)}$ vibration and the three bands assigned to the split $\nu_{3(SO_4)}$ mode (Chio et al. 2007) slightly decrease in wavenumber position with increasing $x_{Ni}$, in accord with the observed slight relaxation of the $SO_4^{2-}$ tetrahedron reflected in the elongation of S–O bond lengths toward dwornikite (Figs. 3c and 4a; Table 6). Of the three bands assigned to the $\nu_{3(SO_4)}$ vibration, only the major one is depicted and its position followed in Figure 9a and Table 8. In contrast to the diverging trends found for the hydrogen bonding schemes and O–H stretching vibrations, the structural and spectroscopic sulfate behavior upon Ni uptake is closely comparable with the situation recently investigated (Talla and Wildner 2019) for Fe uptake in the kieserite–szomolnokite series (Figs. 9a and 9b). The prominent absorption band at ~900 cm$^{-1}$ deemed as "diagnostic"

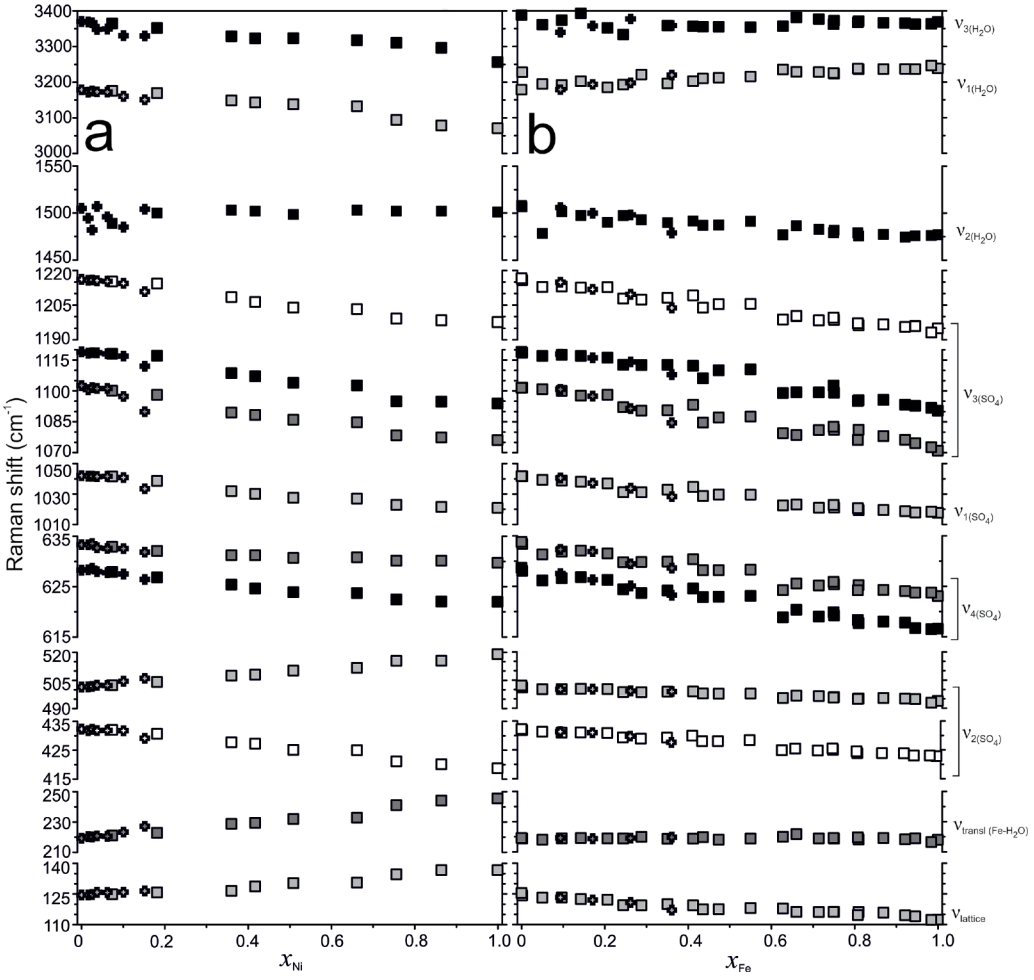


**Figure 12.** Dependence of the Raman band positions in the $Mg_{1-x}Me_x(SO_4)\cdot H_2O$ solid-solution series on (**a**) the Ni content and on (**b**) the Fe content at room temperature. Errors are equal or smaller than the symbol size. Data for the Mg-Fe solid solution are taken from Talla and Wildner (2019). Cross symbols in **a** differentiate between samples obtained hydrothermally with a fully sealed autoclave from those prepared by the evaporation technique (squares), while crosses in **b** discern the use of a metallic Fe redox buffer from $H_2SO_3$.

**Table 9.** Positions of relevant bands in Raman spectra for the kieserite and dwornikite end-members, $Mg/Ni(SO_4)\cdot H_2O$

| Peak assignment | Raman shift position at RT ($cm^{-1}$) | | Linear regression coefficients[a] | | Band shift with temperature decrease |
|---|---|---|---|---|---|
| | Kieserite | Dwornikite | *a* | *b* | ($\times 10^{-2}$ $cm^{-1}$/°C) |
| Lattice modes | 125.3(1) | 136.7(8) | 12.4(8) | 124.3(4) | 0.026 |
| $n_{transl\ Fe\text{-}H_2O}$ | 219.2(1) | 245.57(7) | 26(1) | 219.6(6) | 0.013 |
| $n_{2(SO_4)\_1}$ | 432.2(1) | 418.75(6) | –13.8(6) | 432.6(3) | –0.004 |
| $n_{2(SO_4)\_2}$ | 502.1(1) | 519.0(5) | 16.8(6) | 501.7(3) | 0.019 |
| $n_{4(SO_4)\_1}$ | 628.7(4) | 622.0(2) | –7.1(4) | 628.2(2) | 0.006 |
| $n_{4(SO_4)\_2}$ | 633.8(2) | 629.7(1) | –3.5(3) | 633.0(1) | –0.003 |
| $n_{1(SO_4)}$ | 1041.8(1) | 1020.88(1) | –23(1) | 1042(1) | –0.003 |
| $n_{3(SO_4)\_1}$ | 1101.6(1) | 1076.06(6) | –27(1) | 1101(1) | –0.012 |
| $n_{3(SO_4)\_2}$ | 1118.9(1) | 1093.87(4) | –27(1) | 1119(1) | 0.011 |
| $n_{3(SO_4)\_3}$ | 1216.7(1) | 1197.69(7) | –20.4(9) | 1216(1) | 0.061 |
| $n_{2(H_2O)}$ | 1508.3(1) | 1501.2(8) | 8(5) | 1496(2) | 0.018 |
| $n_{1(H_2O)}$ | 3178(2) | 3071(5) | –101(7) | 3179(3) | –0.481 |
| $n_{3(H_2O)}$ | 3388(4) | 3257(25) | –82(9) | 3361(4) | 0.162[b] |

*Notes:* Linear regression coefficients of the correlation between the band position and the Ni-content ($x_{Ni}$) are listed. Additionally, changes in the band position with decreasing temperature are given for all relevant Raman bands.
[a] Linear regression equation $y = \mathbf{a}(x_{Ni}) + \mathbf{b}$, where *y* denotes the Raman shift position.
[b] High uncertainty.

by Lane et al. (2015) shows a pronounced wavenumber increase toward Ni-rich compositions, as opposed to its behavior upon Fe uptake (Figs. 9a and 9b). This band is usually assigned to a librational mode of the $H_2O$ molecule (e.g., Lane 2007; Lane et al. 2015), which is supported by its contradicting behavior in case of the Mg-Fe and Mg-Ni solid solutions, such as in the case of the $H_2O$ stretching modes. Alternatively, considering the low-temperature behavior described below, the band may also be attributed to a combination mode of the sulfate and octahedral vibration modes (Talla and Wildner 2019). A group of bands at ~630 $cm^{-1}$ (Fig. 7), assigned by Lane et al. (2015) to the $\nu_{4(SO_4)}$ vibration, can hardly be exploited for cosmochemical considerations, as the spectral region not only consists of numerous peaks with varying FWHM, but also is not clearly discernible from the signals of other sulfates (Cloutis et al. 2007) and also of atmospheric $CO_2$. Therefore, the IR spectral region between 700 and 300 $cm^{-1}$ (14.3–27.0 μm) was not studied in further detail.

Contrarily, the 4400–5200 $cm^{-1}$ (2.27–1.92 μm) spectral region where combination modes of the $H_2O$ stretching and

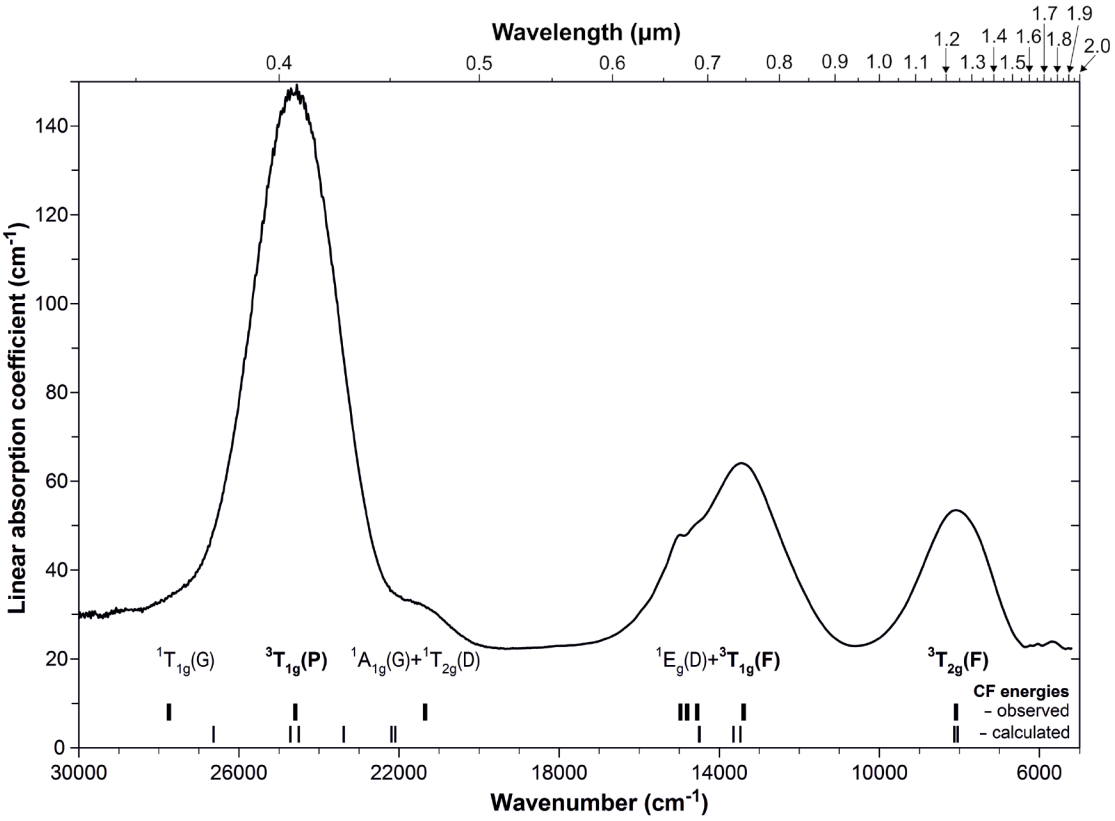


**Figure 13.** UV-Vis-NIR absorption spectrum of dwornikite in the range from 30 000–5000 $cm^{-1}$ with observed (bold line marks) and calculated energy levels (thin line marks) and respective assignments for cubic symmetry.

bending vibrations induce absorptions is considered by many authors to be an important spectral signature in reflectance spectra, allowing the kieserite to be discerned from other sulfate hydrates in which these bands occur at higher wavenumbers (Mangold et al. 2008; Noel et al. 2015) but also to roughly infer either its Fe content (Cloutis et al. 2007; Bishop et al. 2009; Liu et al. 2016; Talla and Wildner 2019) or Ni content (this work), due to the opposite behavior of the respective group of bands in the two binary sulfate monohydrate solid solutions. The $H_2O$ combination modes are most apparent in diffuse reflectance spectra measured on undiluted sample material, whereas they are largely suppressed and too faint to be tracked effectively in the other measuring modes. The kieserite end-member shows a typical set of three bands at 4688, 4845, and 5087 $cm^{-1}$ (2.13, 2.06, and 1.96 μm) (Figs. 8a and 8b; Table 8). The two lower-energetic components decrease significantly to 4566 and 4735 $cm^{-1}$ (2.19 and 2.11 μm), respectively, in the dwornikite end-member, whereas the peak at the highest wavenumber increases to 5110 $cm^{-1}$ (Fig. 8a). In the case of Fe-rich solid solutions and pure szomolnokite, the peripheral bands show opposite behavior, converging to the central one while largely maintaining the overall spectral position of the triplet. The highest-energetic band is always weak, even creating the misleading impression of a single broad absorption in the case of szomolnokite, since it occurs as a weak shoulder in the band group (Talla and Wildner 2019).

The afore-mentioned impact of the sample dilution on DRIFT spectra and their artifacts has important implications for orbiter measurements, where IR spectra reflected by "fluffy" kieserite aggregates (more transmission) would somewhat differ in shape and band position from signals acquired on compact kieserite masses or crusts due to the different reflection/transmission ratio of the particular material. Disregard of these issues could complicate

**Table 10.** Summary of results from classical crystal field (CF) and superposition model (SM) calculations for $Ni^{2+}$ in dwornikite, based on observed transitions energies as indicated in Figure 13

| Szomolnokite | SM (triclinic) | "Classical" CF (tetragonal) |
|---|---|---|
| $Dq_{cub}$ | – | 810 |
| $Dq_{eq}$ | – | 804 |
| Dt | – | –10[a] |
| Ds | – | –120 |
| Racah *B* | 920 | 920 |
| Racah *C* | 4.2B[b] | 3860 |
| β ($B_0$ = 1042 $cm^{-1}$) | 0.88 | 0.88 |
| $Dq_{cub}$ (from $s_4$) | 813 | 810 |
| $\bar{B}_4$ | 4920 | – |
| $t_4$ | 0.8[b] | – |
| $\bar{B}_2$ | 250[b] | – |
| $s_4$ | 7448 | 7424 |
| $s_2$ | 51 | 376 |

*Notes:* Fixed SM parameters are $R_0$ = 2.06 Å, $t_2$ = 3. All given values are in $cm^{-1}$ except the nephelauxetic ratio β. Racah $B_0$ is taken from Figgis and Hitchman (2000).
[a] See text.
[b] Fixed.

the assessment of the properties and composition of the measured monohydrate sulfate. On the contrary, the grain size seems to have little effect on band *position* in IR reflectance spectra (Jamieson et al. 2014; Pitman et al. 2014).

According to their divergent behavior in the IR spectra, the $H_2O$-related bands allow us to easily discern between Fe or Ni enrichment in the ideal case of a purely binary $Mg_{1-x}Me_xSO_4 \cdot H_2O$ solid solution at ambient temperature (Table 8). In the case of Ni contents, the wavenumbers of the $H_2O$ stretching modes $\nu_{1(H_2O)}$ and $\nu_{3(H_2O)}$ are always lower than in end-member kieserite. Conversely, respective Fe enrichment is indicated by a higher wavenumber mainly of the $\nu_{1(H_2O)}$ stretching vibration compared to pure kieserite (Talla and Wildner 2019, Figs. 9a and 9b). In addition, the $H_2O$ combination mode region centered at ~4900 $cm^{-1}$ (2.04 μm) in DRIFT spectra is a further promising candidate for the assessment of Ni or Fe contents, due to the opposite behavior of the peripheral bands (Fig. 8, Table 8). Likewise, the band at ~900 $cm^{-1}$ (11.1 μm) is another candidate allowing to discern between Fe or Ni contents since it increases in wavenumber by 57 $cm^{-1}$ in case of Ni uptake toward the dwornikite end-member, but decreases by roughly 50 $cm^{-1}$ in szomolnokite in respect to the kieserite end-member benchmark. The $H_2O$ bending vibration as well as the sulfate modes all show but minor changes in respect to the sample chemistry. These are comparable irrespective of the transition element substituting Mg (Figs. 9 and 9b).

**Temperature dependence of IR spectra.** The discussion so far was limited to room-temperature data. However, temperature-related changes are to be expected, not only for data from Mars (+20 to –120 °C at latitudes <40°; Witzke et al. 2007) but especially considering the situation on the icy moons of Jupiter and Saturn with mean equatorial surface temperature in the range of 90–100 K (e.g., on Europa, Ashkenazy 2019). The structural changes upon temperature decrease are similar for dwornikite (Tables 4 and 7), kieserite, and szomolnokite (Talla and Wildner 2019), without any indication of a phase transition in either case. Examining and comparing the respective acquired low-temperature IR-spectra (Figs. 10a and 10b), two aspects are evident. First, all vibrations related to the sulfate group are more or less stable in their wavenumber position regardless of temperature across either solid solution, confirming their rigid character, regardless of the element substituting Mg. The $H_2O$-related symmetric stretching vibration shows a comparable decrease in wavenumber position for the Mg-Ni and Mg-Fe solid solutions (Talla and Wildner 2019), irrespective of composition. The band at ~900 $cm^{-1}$ in the Mg-Ni solid solution and at ~850 $cm^{-1}$ in the Mg-Fe series (Figs. 10a and 10b) shows a wavenumber increase by about 0.07 $cm^{-1}$/°C across the +40 °C to –180 °C temperature range in both solid solutions. The parallel response to temperature decrease, along with the inverted correlation trends upon Ni- or Fe- incorporation in accord with the behavior of the $H_2O$ stretching modes, strongly hint this band to be linked to an $H_2O$-related (librational) mode.

Surprisingly, the $H_2O$ bending vibration remains nearly unaffected upon cooling (Figs. 10a and 10b), indicating no major influence of temperature on the internal molecular structure of the water molecule, thus corroborating its "rigid" character. Accordingly, the acceptor-donor-acceptor angle O2–O3–O2 is insensitive to temperature (–1.0° change along 200 K), compared to the significant influence of the Mg/Ni ratio (–3° change).

**Raman spectra at ambient conditions.** Raman spectra acquired across the Mg-Ni solid-solution series also show systematic band shifts with increasing $x_{Ni}$ (Figs. 11a and 12, Table 9). The linear trends and wavenumber shifts of related vibrational phenomena observed in Raman spectra basically correspond to their behavior in FTIR spectra.

As expected, the decrease in hydrogen bond length with increasing Ni content reported above leads to the decrease in the wavenumber of the $H_2O$ symmetric stretching vibration from 3178 to 3071 $cm^{-1}$ shift and that of the antisymmetric mode from 3388 to 3257 $cm^{-1}$. The very good match between the wavenumber position observed in the IR transmission spectra (Table 8) and Raman data (Table 9) underline the consistency of both sets of data. The decrease in shift of the antisymmetric $\nu_{3(H_2O)}$ vibration is well visible in case of the Mg-Ni solid solution (Fig. 12a), in analogy to the FTIR spectra (Fig. 10a), despite its position as a weak shoulder of the dominant $\nu_{1(H_2O)}$ vibration. This is in sharp contrast to the kieserite-szomolnokite solid solution (Fig. 12b), where no observable trend could be identified for the $\nu_{3(H_2O)}$ mode (Talla and Wildner 2019). This contrast can be attributed to the much larger change of the hydrogen bond length between the kieserite and dwornikite end-members (–0.068 Å) (Fig. 4c) compared to the respective difference between kieserite and szomolnokite (+0.012 Å; Talla and Wildner 2019).

The nearly perfect match between the behavior of the sulfate group in the Mg-Ni and Mg-Fe kieserite solid solution, including the absolute positions of the corresponding sulfate-related bands (Fig. 12), is remarkable. This is in agreement with the relaxation of the sulfate tetrahedron (Figs. 3c and 3d, Table 6) both in case of Fe and Ni incorporation (Talla and Wildner 2019). On the other hand, the assignment of the band at 500 $cm^{-1}$ to sulfate-related modes by Chio et al. (2007) is disputable, since this band shows opposite behavior in both solid solutions (Fig. 12).

The bands observed in the 100–250 $cm^{-1}$ spectral region feature a component at ~220 $cm^{-1}$ assigned by Chio et al. (2007) to a vibration involving the translation along the Fe–$H_2O$ bond in szomolnokite. However, its spectral position remains nearly unchanged regardless of the Mg/Fe ratio (Fig. 12b). A much larger variation (an increase in wavenumber) is found for the corresponding band in the case of Ni uptake (Fig. 12a, Table 9). Presuming the involvement of the $H_2O$ molecule in the given Raman mode, more pronounced changes are indeed to be expected in the case of the Mg-Ni solid solution, since, as was already mentioned, the hydrogen bonding system undergoes much larger changes. (Figs. 9a, 9b, 12a, and 12b and Tables 8 and 9; Fig. 4c and Table 6). For the lowest mode at ~130 $cm^{-1}$ a contradicting behavior in the case of Ni and Fe incorporation is observed. While we are unable to ascertain the exact character of this vibrational mode, this difference suggests the involvement of octahedral modes, since these polyhedra also show opposite structural trends between the Mg-Ni solid solution (decrease in polyhedral volume and Me–O2,O3 bond lengths) and the Mg-Fe series (increase in polyhedral volume and all Me–O bonds).

**Raman spectra at low-temperature conditions.** Band shifts in low-temperature Raman spectra show similar behavior to corresponding vibrational modes in the IR spectra (Table 9), and comparison with previous data for the Mg-Fe solid solution (Talla and Wildner 2019) reveal that they are largely independent

of the cation substituting for Mg. As expected, the $\nu_{1(H_2O)}$ vibration shows significant changes toward lower shift values upon cooling, while the sulfate-related bands are stable. Better band resolution compared to IR spectra allows tracking even the subtle positional changes of these peaks. The highest-energy peak at ~1200 $cm^{-1}$ of the split $\nu_{3(SO_4)}$ vibration takes higher shift values, while a decrease in position for the lowest-situated $\nu_{3(SO_4)}$ peak at ~1100 $cm^{-1}$ shift can be observed (Table 9). The symmetric stretching vibration $\nu_{1(SO_4)}$ shows a very minor decrease in wavenumber (Table 9). The octahedra-related mode at ~220 $cm^{-1}$ exhibits a notable increase in wavenumber at low temperature, as does the lattice band at ~130 $cm^{-1}$. The complex nature of this low-energy lattice mode does not allow reliable band assignment without ab initio calculations, beyond the scope and aim of the present study.

**Use of vibrational spectra to estimate Ni- and Fe-contents of (extraterrestrial) kieserite.** Linear trends, observed for changes in structural parameters across the kieserite-dwornikite solid solution (Figs. 2–4), as well as in the position of IR spectral bands (when expressed in wavenumber units) and Raman spectra, clearly correlate with the Mg/Ni ratio (Figs. 9 and 11). Aside from documenting in detail the behavior of kieserite-group compounds throughout the Mg-Ni solid-solution series relevant to the icy moons of Jupiter and Saturn, the linearity of the data also allows its straightforward use as a standard of comparison in evaluating IR spectra acquired by orbiters, as well as Raman measurements that could be conducted during eventual rover missions. In this regard, the use of wavelength units (in μm) to express spectral band positions, as it is common in the cosmochemical community, would seem to be more appropriate. However, our preference for—and the benefits of—the use of wavenumber units ($cm^{-1}$) throughout this work for discussion and depiction of spectroscopic data have been amply discussed in our previous paper (Talla and Wildner 2019).

In general, the evaluation of orbiter measurements in the VNIR-MIR spectral range (visible to near/medium infrared) leading to the assessment of the mineral phases present on the surface of celestial bodies and their composition follows the "spectral unmixing" approach, requiring reference end-member spectra, as is the case in the currently conducted investigations of surface spectra from Mars (Cloutis et al. 2007; Combe et al. 2008; Mangold et al. 2008; Bishop et al. 2009; Lichtenberg et al. 2010; Roach et al. 2010; Noel et al. 2015; Liu et al. 2016). In brief, spectra from orbiter measurements are fitted by the least-squares technique using reference end-member spectra to fit the measured signal after its correction for the instrumental function (CRISM smile, etc.), atmospheric scattering (if relevant), and the incidence angle using detailed knowledge of the local topography. While to this date, only pure end-member kieserite spectra were used for this assessment, the discovery of linear trends across the kieserite-dwornikite solid solution presented in this work as well as across the kieserite-szomolnokite solid solution (Talla and Wildner 2019) allows deriving reference spectra for monohydrate sulfates of an intermediate composition and, in principle, obtaining additional information on the chemistry (Mg/Ni ratio in the present case) of the kieserite-group sulfate monohydrate at hand, with semi-quantitative results at least. Two prominent features in the IR spectra, which show a pronounced slope in their correlation with increasing Ni content, are the symmetric and antisymmetric stretching vibration $\nu_{1(H_2O)}$ and $\nu_{3(H_2O)}$ of $H_2O$, with a negative correlation to $x_{Ni}$, and the "diagnostic" band at ~900 $cm^{-1}$, the wavenumber of which increases with Ni content in contrast to the situation in the Mg-Fe solid solution (Figs. 9 and 12b, Table 8). The fact that the antisymmetric stretching mode $\nu_{3(H_2O)}$ of the $H_2O$ molecule shows a clear dependence on the Ni content can be regarded as an important benchmark, allowing one to discern between Ni- and Fe-incorporation, since no such trend is observed in case of Fe contents along the Mg-Fe solid solution (Talla and Wildner 2019). However, the two other promising features to infer the Ni content in the medium-infrared region—$\nu_{1(H_2O)}$ and the diagnostic band at ~900 $cm^{-1}$, which show opposite behavior compared to the Mg-Fe solid solution—are also the ones that show the largest change in wavenumber with decreasing temperature (Fig. 10). The same, considering the temperature sensitivity of the fundamental $H_2O$ bands, will apply to their combination modes in the ~4900 $cm^{-1}$ region (Figs. 8a amd 8b), which, according to the results for kieserite of Jamieson et al. (2014), split further apart with decreasing temperature. This behavior enhances the splitting of those bands in addition to the effect of Ni incorporation, leading to a potential overestimation of $x_{Ni}$. Despite being the exact opposite to the merging of these bands into a seemingly single broad absorption with a shoulder upon Fe intake (Talla and Wildner 2019), the influence of temperature complicates a reliable assessment of Ni contents in the examined material.

Anyway, the knowledge of surface temperatures (at least approximate values) during remote measurements is a prerequisite to allow for meaningful quantitative comparisons, otherwise only semi-quantitative information may be extracted. The rough estimation of temperature is in part possible even from remote sensing spectra in themselves because they contain spectral regions that slightly shift according to the surface temperature, such as the ~5000 $cm^{-1}$ (2 μm) wavenumber region (Liu et al. 2016). Mid-infrared hyperspectral remote sensing instruments (and bolometers) can provide radiance data. Because these follow Planck behavior, they can easily be converted to emissivity by the application of a Planck function at a given temperature, to provide accurate surface temperature values (for references see, e.g., Ruff et al. 1997). In addition, any rovers, whether in the scope of present (Mars) or future (e.g., the Jovian moons) missions, are typically equipped with thermometers, providing an additional rough temperature value. The attempt to use sulfate-related bands for such considerations is hampered by their wavenumber position being largely insensitive to temperature changes in the IR spectra regardless of the substituting cation (Fe vs. Ni), as can be seen in Figures 10a and 10b. This will likely prevent any exact observation of the subtle band position changes also due to enhanced noise.

Additional sources of error arise from the use of different correction data sets preceding the actual spectral unmixing procedure. Different versions of the atmospheric correction model used in the evaluation of CRISM spectra from Mars may lead to significant changes in the form of the resulting spectrum, even causing errors in the discrimination between kieserite and szomolnokite in the same region of interest (Bishop et al. 2009; Noel et al. 2015).

A much more promising situation is to be expected considering the high resolution and low FWHM of Raman bands, which aids in ascertaining their position changes from kieserite to dwornikite with much higher precision when the Raman spectrometer is close to the target (i.e., not from an orbital platform). While the superior

spectral resolution allows efficient use of the sulfate-related bands, such as the prominent $\nu_{1(SO_4)}$ band (Fig. 11), it is possible to derive the *total* Mg/$Me^{2+}$ ($Me^{2+}$ = $Fe^{2+}$ + $Ni^{2+}$) content only, because the sulfate modes behave analogically in the case of Ni or Fe uptake, as opposed to the $H_2O$ stretching vibrational modes, that show opposite trends between Ni and Fe incorporation (Figs. 12a and 12b, respectively). These water bands are, however, weaker in the Raman spectra (Fig. 11) and are temperature-sensitive.

Further complications arise if a ternary Mg/Fe/Ni solid solution is present. As described above, the major difference in vibrational spectra of the Mg-Fe (Talla and Wildner 2019) and Mg-Ni solid solution (this work) concerns the vibrational modes involving the $H_2O$ molecule (Figs. 9a and 9b). Structurally induced opposite trends are observed for both $H_2O$ stretching modes. In the case of Fe uptake, mainly the symmetric $\nu_{1(H_2O)}$ mode undergoes changes, shifting to higher wavenumbers as the O3···O2 donor–acceptor distance increases. This shift would be dampened by the presence of Ni in a ternary solid solution. Fortunately, the antisymmetric $\nu_{3(H_2O)}$ mode remains constant in position regardless of the Mg/Fe ratio (at ~3380 $cm^{-1}$ in FTIR transmission mode), whereas a prominent decrease of its position occurs in case of Ni-incorporation, as shown in Figures 9a and 9b. This opens up the chance to discriminate between Ni and Fe contents in kieserite: taking the position of the antisymmetric $H_2O$ stretching mode $\nu_{3(H_2O)}$ as a reference to derive the Ni content, the Fe content may as well be estimated, based on the difference between the position of the symmetric $\nu_{1(H_2O)}$ stretching mode expected from the deduced Ni formula content, and its actual position, expectably at somewhat higher wavenumbers (indicative of Fe content).

The total content of both transition elements (Ni and Fe) can, in theory, be verified via the sulfate-related bands in Raman spectra if these are available (preferably using the strongest $\nu_{1(SO_4)}$ band), because their positions are insensitive to temperature (see above and Talla and Wildner 2019). They undergo the same changes to lower shift values, irrespective of the transition element present.

**Crystal field spectra.** The crystal field (CF) spectrum of dwornikite (Fig. 13) shows that VNIR spectra from orbiter or rover measurements might be influenced by Ni contents of monohydrate sulfates, in particular by the broad first spin-allowed $^3A_{2g}(F) \rightarrow {}^3T_{2g}(F)$ band, at ambient conditions centered at ~8100 $cm^{-1}$ (~1.24 μm), but extending from 6400 to 10 400 $cm^{-1}$ (1.57 to 0.95 μm). Besides, a Superposition Model (SM) calculation applying the ambient SM parameters from Table 10 to the octahedral $NiO_6$ geometry at –160 °C (Table 7) reveals that temperature-dependent band shifts are expected to be negligible, i.e., 10 $cm^{-1}$ for $^3T_{2g}(F)$ to at most 20 $cm^{-1}$ for the two higher-energetic $^3T_{1g}$ bands.

In agreement with the absence of any perceivable band splitting, at least for the first and third spin-allowed band (Fig. 13), the obtained CF and SM parameters do not properly reproduce the structural [4+2] elongation of the $NiO_6$ octahedron. In fact, with Dt = –10 $cm^{-1}$ even a faint polyhedral compression of the pseudo-tetragonal axis is indicated. This discrepancy can be best explained by the higher CF strength of $H_2O$ ligands forming the elongated axis (compared to the oxygen ligands of the sulfate groups), in this way obviously fully compensating the structural elongation. A similar but less pronounced partial compensation effect was also found in the CF spectra of cobaltkieserite (Wildner 1996) and szomolnokite (Talla and Wildner 2019). The same reasoning may also be applicable to some of the extracted SM parameters, namely $t_4$ and $\overline{B}_2$, which yielded quite unrealistic low values. Albeit, a tendency toward $t_4$ values much lower than their electrostatic ideal value ($t_4$ = 5) has been observed previously for divalent transition metal compounds, among them also cobaltkieserite (Andrut et al. 2004).

## Implications

The presented data for the kieserite-dwornikite solid solution can assist cosmochemical investigations, given the presence of kieserite-group sulfates on the surface of Mars and potentially on the Jovian moons, where conditions are favorable for their formation. The linear character of the observed spectral and structural trends at room temperature and the knowledge of their changes upon cooling provides a solid starting basis to draw conclusions about the content of Ni in kieserite based on absorption band positions in IR and Raman spectra. Even in the unfavorable case of a semi-quantitative approach (no knowledge of temperature), zoning of Ni contents in kieserite-containing sediments can be monitored using the presented data. Given the change in the spectral position of the antisymmetric $H_2O$ vibration occurring only upon Ni-incorporation, a good chance to reliably estimate Ni vs. Fe contents in a ternary Mg-Fe-Ni-kieserite solid solution presents itself as well, presuming at least a rough knowledge of the surface temperature on the investigated planetary body.

## Acknowledgments and Funding

We thank R. Miletich, M. Ende, and J. Meusburger (all Vienna) for helpful discussions. Assistance by G. Giester (Vienna) with the low-temperature X-ray data collections is gratefully acknowledged. M.W. is grateful to Y.Y. Yeung (Hong Kong) for providing a modified copy of his HCFLDN2 program. We thank the reviewers Henrik Skogby and Melissa Lane for their constructive approach, which improved the quality of this paper in many ways. This work was supported by a grant from the Austrian Science Fund (FWF): P 29149-N29.

## References cited

Anders, E., and Grevese, N. (1989) Abundances of the elements: Meteoritic and solar. Geochimica et Cosmochimica Acta, 53, 197–214.

Andrut, M., Wildner, M., and Rudowicz, C.Z. (2004) Optical absorption spectroscopy in geosciences. Part II: Quantitative aspects of crystal fields. In A. Beran and E. Libowitzky, Eds., Spectroscopic Methods in Mineralogy, p. 145–188. EMU Notes in Mineralogy 6, Eötvös Univ Press, Budapest.

Ashkenazy, Y. (2019) The surface temperature of Europa. Heliyon, 5, e01908, 1–11.

Bechtold, A., and Wildner, M. (2016) Crystal chemistry of the kieserite–cobaltkieserite solid solution, $Mg_{1-x}Co_x(SO_4)\cdot H_2O$: well behaved oddities. European Journal of Mineralogy, 28, 43–52.

Bishop, J.L., Parente, M., Weitz, C.M., Noe Dobrea, E.Z., Roach, L.H., Murchie, S.L., McGuire, P.C., McKeown, N.K., Rossi, C.M., Brown, A.J., and others. (2009) Mineralogy of Juventae Chasma: Sulfates in the light-toned mounds, mafic minerals in the bedrock, and hydrated silica and hydroxylated ferric sulfate on the plateau. Journal of Geophysical Research, 114, E00D09.

Brese, N.E., and O'Keeffe, M. (1991) Bond-valence parameters for solids. Acta Crystallographica, B47, 192–197.

Brown, I.D., and Shannon, R.D. (1973) Empirical bond–strength–bond–length curves for oxides. Acta Crystallographica, A29, 266–282.

Burgess, R., Wright, I.P., and Pillinger, P.T. (1991) Determinations of sulphur-bearing components in C1 and C2 carbonaceous chondrites by stepped combustion. Meteoritics, 26, 55–64.

Chang, Y.M., Rudowicz, C., and Yeung, Y.Y. (1994) Crystal field analysis of the $3d^N$ ions at low symmetry sites including the "imaginary" terms. Computers in Physics, 8, 583–588.

Chio, C.H., Sharma, S.K., and Muenow, D.W. (2007) The hydrates and deuterates of ferrous sulfate ($FeSO_4$): a Raman spectroscopic study. Journal of Raman Spectroscopy, 38, 87–99.

Cloutis, E.A., Craig, M.A., Mustard, J.F., Kruzelecky, R.V., Jamroz, W.R., Scott, A., Bish, D.L., Poulet, F., Bibring, J.-P., and King, P.L. (2007) Stability of hydrated minerals on Mars. Geophysical Research Letters, 34, L20202.

Combe, J.-Ph., Le Mouélic, S., Sotin, C., Gendrin, A., Mustard, J.F., Le Deit, L., Launeau, P., Bibring, J.-P., Gondet, B., Langevin, Y., and Pinet, P. (2008) Analysis of OMEGA/Mars Express hyperspectral data using a Multiple-Endmember Linear Spectral Unmixing Model (MELSUM): Methodology and first results. Planetary

and Space Science, 56, 951–975.
Dalton, J.B., Prieto-Ballesteros, O., Kargel, J.S., Jamieson, C.S., Jolivet, J., and Quinn, R. (2005) Spectral comparison of heavily hydrated salts with disrupted terrains on Europa. Icarus, 177, 472–490.
Dalton, J.B., Shirley, J.H., and Kamp, L.W. (2012) Europa's icy bright plains and dark linea: Exogenic and endogenic contributions to composition and surface properties. Journal of Geophysical Research, 117, E03003.
Downs, R.T., Gibbs, G.V., Bartelmehs, K.L., and Boisen, M.B. Jr. (1992) Variations of bond lengths and volumes of silicate tetrahedra with temperature. American Mineralogist, 77, 751–757.
Ende, M., Kirkkala, T., Loitzenbauer, M., Talla, D., Miletich, R., and Wildner, M. (2019a) Pressure induced phase transitions of dwornikite. Zeitschrift für Kristallographie Supplement, 39, 60–61.
Ende, M., Loitzenbauer, M., Matzinger, P., Meusburger, J., Talla, D., Miletich, R., and Wildner, M. (2019b) Pressure induced phase transition in $CoSO_4 \cdot H_2O$. Book of Abstracts of the 32nd European Crystallographic Meeting, 284.
Figgis, B.N., and Hitchman, M.A. (2000) Ligand Field Theory and its Applications, 364 p. Wiley-VCH, New York.
Frederiksson, K., and Kerridge, J.F. (1988) Carbonates and sulphates in C1 chondrites: Formation by aqueous activity on the parent body. Meteoritics, 23, 35–44.
Hawthorne, F.C., Groat, L.A., Raudsepp, M., and Ercit, T.S. (1987) Kieserite, $Mg(SO_4)(H_2O)$, a titanite-group mineral. Neues Jahrbuch für Mineralogie Abhandlungen, 157, 121–132.μ
Griffen, D.T., and Ribbe, P.H. (1979) Distortions in the tetrahedral oxyanions of crystalline substances. Neues Jahrbuch Mineralogischer Abhandlungen, 137, 54–73.
Jamieson, C.S., Noe Dobrea, E.Z., Dalton, J.B. III, Pitman, K.M., and Abbey, W.Z. (2014) The spectral variability of kieserite ($MgSO_4 \cdot H_2O$) with temperature and grain size and its application to the Martian surface. Journal of Geophysical Research: Planets, 119, 1218–1237.
Journaux, B., Daniel, I., Petitgirard, S., Cardon, H., Perrillat, J.-P., Caracas, R., and Mezouar, M. (2017) Salt partitioning between water and high-pressure ices. Implication for the dynamics and habitability of icy moons and water-rich planetary bodies. Earth and Planetary Science Letters, 463, 36–47.
Kargel, J.S. (1991) Brine volcanism and the interior structures of asteroids and icy satellites. Icarus, 94, 368–390.
Kargel, J.S., Kaye, J.Z., Head, J.W. III, Marion, G.M., Sassen, R., Crowley, J.K., Prieto-Ballesteros, O., Grant, S.A., and Hogenboom, D.L. (2000) Europa's crust and ocean: Origin, composition, and the prospects for life. Icarus, 148, 226–265.
Knauth, L.P., Burt, D.M., and Wohletz, K.H. (2005) Impact origin of sediments at the Opportunity landing site on Mars. Nature, 438, 1123–1128.
Lane, M.D. (2007) Mid-infrared emission spectroscopy of sulfate and sulfate-bearing minerals. American Mineralogist, 92, 1–18.
Lane, M.D., Bishop, J.L., Dyar, M.D., Hiroi, T., Mertzman, S.A., Bish, D.L., King, P.L., and Rogers, A.D. (2015) Mid-infrared emission spectroscopy and visible/near-infrared reflectance spectroscopy of Fe-sulfate minerals. American Mineralogist, 100, 66–82.
Libowitzky, E. (1999) Correlation of O–H stretching frequencies and O–H···O hydrogen bond lengths in minerals. Monatshefte für Chemie, 130, 1047–1059.
Lichtenberg, K.A., Arvidson, R.E., Morris, R.V., Murchie, S.L., Bishop, J.L., Fernández-Remolar, D., Glotch, T.D., Dobrea, E.N., Mustard, J.F., Andrews-Hanna, J., and Roach, L.H. (2010) Stratigraphy of hydrated sulfates in the sedimentary deposits of Aram Chaos, Mars. Journal of Geophysical Research, 115, E00D17.
Liu, Y., Glotch, T.D., Scudder, N.A., Kraner, M.L., Condus, T., Arvidson, R.E., Guinness, E.A., Wolff, M.J., and Smith, M.D. (2016) End-member identification and spectral mixture analysis of CRISM hyperspectral data: A case study on southwest Melas Chasma, Mars. Journal of Geophysical Research: Planets, 121, 2004–2036.
Mangold, N., Gendrin, A., Gondet, B., LeMouelic, S., Quantin, C., Ansan, V., Bibring, J.-P., Langevine, Y., Masson, P., and Nukum, G. (2008) Spectral and geologic study of the sulfate-rich region of West Candor Chasma, Mars. Icarus, 194, 519–543.
McCord, T.B., Hansen, G.B., and Hibbits, C.A. (2001) Hydrated salt minerals on Ganymede's surface: Evidence of an ocean below. Science, 292, 1523–1525.
McKinnon, W.B., and Zolensky, M.F. (2003) Sulfate content of Europa's ocean and shell: Evolutionary considerations and some geological and astrobiological implications. Astrobiology, 3, 879–897.
Meusburger, J.M., Ende, M., Talla, D., Miletich, R., and Wildner, M. (2018) Pressure induced second order phase transition in monohydrated magnesium sulphate ($MgSO_4 \cdot H_2O$): A new polymorph potentially occurring on icy satellites. Geophysical Research Abstracts, 20, 8136.
Meusburger, J.M., Ende, M., Talla, D., Wildner, M., and Miletich, R. (2019) Transformation mechanism of the pressure-induced $C2/c$-to-$P\bar{1}$ transition in ferrous sulphate monohydrate single crystals. Journal of Solid State Chemistry, 277, 240–252.
Milton, C., Evans. H.T., and Johnson, R.G. (1982) Dwornikite, $(Ni,Fe)SO_4 \cdot H_2O$, a member of the kieserite group from Minasragra, Peru. Mineralogical Magazine, 46, 351–355.
Nakamura, R., and Ohtani, E. (2011) The high-pressure phase relation of the $MgSO_4$–$H_2O$ system and its implication for the internal structure of Ganymede. Icarus, 211, 648–654.
Noel, A., Bishop, J.L., Al-Samir, M., Gross, C., Flahaut, J., McGuire, P.C., Weitz, C.M., Seelos, F., and Murchie, S. (2015) Mineralogy, morphology and stratigraphy of the light-toned interior layered deposits at Juventae Chasma. Icarus, 251, 315–331.
Papike, J.J., Burger, P.V., Karner, J.M., and Shearer, C.K. (2007) Mars surface mineralogy: Implications of kieserite group crystal chemistry $(Mg,Fe^{2+},Mn^{2+},Zn,Ni,Co)SO_4 \cdot H_2O$. 7th International Conference on Mars, 3004.pdf.
Pitman, K.M., Noe Dobrea, E.Z., Jamieson, C.S., Dalton, J.B. III, Abbey, W.J., and Joseph, E.C.S. (2014) Reflectance spectroscopy and optical functions for hydrated Fe-sulfates. American Mineralogist, 99, 1593–1603.
Powell, R., and Holland, T. (1993) On the formulation of simple mixing models for complex phases. American Mineralogist, 78, 1174–1180.
Roach, L.H., Mustard, J.F., Swayze, G., Milliken, R.E., Bishop, J.L., Murchie, S.L., and Lichtenberg, K. (2010) Hydrated mineral stratigraphy of Ius Chasma, Valles Marineris. Icarus, 206, 253–268.
Robinson, K., Gibbs, G.V., and Ribbe, P.H. (1971) Quadratic elongation: a quantitative measure of distortion in coordination polyhedra. Science, 172, 567–570.
Ruff, S.W., Christensen, P.R., Barbera, P.W., and Anderson, D.L. (1997) Quantitative thermal emission spectroscopy of minerals: A laboratory technique for measurement and calibration. Journal of Geophysical Research, 102, 14899–14913.
Shannon, R.D. (1976) Revised effective ionic radii and systematic studies of interatomic distances in halides and chalcogenides. Acta Crystallographica, A32, 751–767.
Sheldrick, G.M. (2008) A short history of SHELX. Acta Crystallographica, A64, 112–122.
Solomonidou, A., Coustenis, A., Bampasidis, G., Kyriakopoulos, K., Moussas, X., Bratsolis, E., and Hirtzig, M. (2011) Water oceans of Europa and other moons: implications for life in other solar systems. Journal of Cosmology, 13, 4191–4211.
Spencer, J.R., Barr, A.C., Esposito, L.W., Helfenstein, P., Ingersoll, A.P., Jaumann, R., McKay, C.P., Nimmo, F., Porco, C.C., and Waite, J.H. (2009) Enceladus: An active cryovolcanic satellite. In M.K. Dougherty, L.W. Esposito, and S.M. Krimigis, Eds., Saturn from Cassini-Huygens, p. 683–724. Springer.
Stoilova, D. (2003) Influence of the crystal field stabilization energy of metal(II) ions on the structural distortion of matrix-isolated $SO_4^{2-}$ guest ions in selenate matrices. Spectrochimica Acta A, 60, 2243–2251.
Stoilova, D., and Lutz, H.D. (1998) Infrared study of $\nu_{OD}$ modes in isotopically dilute (HDO) kieserite-group compounds $MXO_4 \cdot H_2O$ (M = Mn, Co, Ni, Zn, and X = S, Se) with matrix-isolated $M'^{2+}$ and $X'O_4^{2-}$ guest ions. Journal of Molecular Structure, 450, 101–106.
——— (2002) Infrared study of the vibrational behaviour of the S-O stretching modes in kieserite-group selenates $MeSeO_4 \cdot H_2O$ with matrix-isolated $SO_4^{2-}$ and $Me'^{2+}$ guest ions (Me = Mn, Co, Ni, Zn). Journal of Molecular Structures, 606, 267–272.
Talla, D., and Wildner, M. (2019) Investigation of the kieserite–szomolnokite solid-solution series, $(Mg,Fe)SO_4 \cdot H_2O$, with relevance to Mars: Crystal chemistry, FTIR, and Raman spectroscopy under ambient and martian temperature conditions. American Mineralogist, 104, 1732–1749.
van Hinsberg,V.J., Vriend, S.P., and Schumacher, J.C. (2005a) A new method to calculate end-member thermodynamic properties of minerals from their constituent polyhedra I: Enthalpy, entropy and molar volume. Journal of Metamorphic Geology, 23, 165–179.
——— (2005b) A new method to calculate end-member thermodynamic properties of minerals from their constituent polyhedra II: Heat capacity, compressibility and thermal expansion. Journal of Metamorphic Geology, 23, 681–693.
Vance, S., Bouffard, M., Choukroun, M., and Sotin, C. (2014) Ganymede's internal structure including thermodynamics of magnesium sulfate oceans in contact with ice. Planetary and Space Science, 96, 62–70.
Vegard, L. (1921) Die Konstitution der Mischkristalle und die Raumfüllung der Atome. Zeitschrift der Physik, 5, 17–26.
Wildner, M. (1996) Polarized electronic absorption spectra of $Co^{2+}$ ions in the kieserite-group compounds $CoSO_4 \cdot H_2O$ and $CoSeO_4 \cdot H_2O$. Physics and Chemistry of Minerals, 23, 489–496.
Wildner, M., and Giester, G. (1991) The crystal structure of kieserite-group compounds. I. Crystal structures of $Me^{(II)}SO_4 \cdot H_2O$ (Me = Mn, Fe, Co, Ni, Zn). Neues Jahrbuch für Mineralogie Monatshefte, 296–306.
Wildner, M., Beran, A., and Koller, F. (2013) Spectroscopic characterisation and crystal field calculations of varicoloured kyanites from Loliondo, Tanzania. Mineralogy and Petrology, 107, 289–310.
Witzke, A., Arnold, G., and Stöffler, D. (2007) Spectral detectability of Ca- and Mg-sulphates in Martian bright soils in the 4-5 μm wavelength range. Planetary and Space Science, 55, 429–440.
Zolotov, M.Y., and Shock, E.L. (2001) Composition and stability of salts on the surface of Europan and their oceanic origin. Journal of Geophysical Research, 106, 32,815–32,827.

Manuscript received September 16, 2019
Manuscript accepted February 29, 2020
Manuscript handled by Janice Bishop

## Endnote:

[1]Deposit item AM-20-107287, CIF and Supplemental Material. Deposit items are free to all readers and found on the MSA website, via the specific issue's Table of Contents (go to http://www.minsocam.org/MSA/AmMin/TOC/2020/Oct2020_data/Oct2020_data.html).